PROBABILISTIC HAZARD ASSESSMENT OF TSUNAMIS INDUCED BY THE

TRANSLATIONAL FAILURE OF MULTIPLE SUBMARINE RIGID LANDSLIDES

A Thesis

by

ARTURO JIMENEZ MARTINEZ

Submitted to the Office of Graduate Studies of
Texas A&M University
in partial fulfillment of the requirements for the degree of

MASTER OF SCIENCE

August 2011

Major Subject: Ocean Engineering

Probabilistic Hazard Assessment of Tsunamis Induced by the Translational Failure of

Multiple Submarine Rigid Landslides

PROBABILISTIC HAZARD ASSESSMENT OF TSUNAMIS INDUCED BY THE

TRANSLATIONAL FAILURE OF MULTIPLE SUBMARINE RIGID LANDSLIDES

A Thesis

by

ARTURO JIMENEZ MARTINEZ

Submitted to the Office of Graduate Studies of
Texas A&M University
in partial fulfillment of the requirements for the degree of

MASTER OF SCIENCE

Approved by:

Chair of Committee,	Patrick J. Lynett
Committee Members,	James M. Kaihatu
	Robert Weiss
Head of Department,	John Niedzwecki

August 2011

Major Subject: Ocean Engineering

ABSTRACT

Probabilistic Hazard Assessment of Tsunamis Induced by the Translational

Failure of Multiple Submarine Rigid Landslides. (August 2011)

Arturo Jimenez Martinez, B.S., Jackson State University

Chair of Advisory Committee: Dr. Patrick J. Lynett

A numerical study aimed at probabilistically assessing the coastal hazard posed by tsunamis induced by one-dimensional submarine rigid landslides that experience translational failure is presented. The numerical model here utilized is the finite-difference recreation of a linear, fully dispersive mild-slope equation model for wave generation and propagation. This recreated model has the capability to simulate submarine landslides that detach into multiple rigid pieces as failure occurs. An ad-hoc formulation describing the combined space-time coherency of the landslide is presented. Monte Carlo simulations are employed, with an emphasis on the shoreward-traveling waves, to construct probability of exceedance curves for the maximum dimensionless wave height from which wave statistics can be extracted. As inputs to the model, eight dimensionless parameters are specified both deterministically in the form of parameter spaces and probabilistically with normal distributions. Based on a sensitivity analysis, the results of this study indicate that submarine landslides with large width to thickness ratios and coherent failure behavior are most effective in generating tsunamis. Failures modes involving numerous slide pieces that fail in a very compact fashion, however, were observed to induce bigger waves than more coherent landslides. Rapid weakening in tsunami generation potential for some of the parameter combinations suggests that the hazard posed by submarine landslide tsunamis is strongly dependent on source features and local conditions and is only of concern for landslides of substantial dimensions.

DEDICATION

To my family for the incessant moral and spiritual support that they have given me over the last six years

ACKNOWLEDGEMENTS

NOMENCLATURE

a_o	Initial acceleration of slide
A	Area of submerged slide
b	Slide width parallel to slope
b'	Slide width along slope to slide thickness ratio, dimensionless
b_h	Horizontal width of slide
BEM	Boundary element method
BIEM	Boundary integral equation model
c	Wave celerity
cg	Wave group velocity
C_m	Added-mass coefficient
C_d	Drag coefficient
delay	Scaling factor delimiting the time taken for the slide at rest to fail into Nc pieces, dimensionless
Δf	Frequency resolution, units of hertz
Δh	Slide thickness
doI	Baseline water depth to thickness ratio above slide centre point, dimensionless
ds	Horizontal distance traveled by slide, function of time
ds/dt	Slide center of mass velocity
ellip	Horizontal water depth profile, function of space and time
f	Kinematic field variation with depth

ff_L	Frequency filter function dependent of landslide wave number
ff_W	Frequency filter function dependent of wave number
f_q	Temporal frequency, units of hertz
F,G	Auxiliary variables in MSE derivation
FFT	Fast Fourier transform
FTCS	Forward-time, centered-space
g	Gravity
h	Local water depth, function of space and time
h_c	Baseline water depth above slide centre point
h_{Nc}	Combined water depth of disjoined slide pieces, function of space and time
h_o	Baseline water depth, function of space
h_p, h'_p	Water depth representing slide passage, function of space and time
h_t	Time-domain forcing function of MSE model
h_{tt}	Frequency-domain forcing function of MSE model
h_F	Fourier transform in time of h, function of space and frequency
$H_{max}/\Delta h$	Maximum wave height, dimensionless
$H_{0.05}$	Wave height with 5% exceedance probability, dimensionless
$\hat{i}$	Imaginary number ($\sqrt{-1}$)
k	Wave number
k_s	Landslide wave number
L_s	Landslide characteristic length

L_1, L_2	Landslide characteristic sides
MSE	Mild-slope equation
nt	Number of time steps in numerical model
nx, ny	Number of space steps in numerical model
N	Fourier transform in time of η, function of space and frequency
Nc	Integer number of pieces detaching from slide at rest
NGDC/WDC	National Geophysical Data Center / World Data Center
NOAA	National Oceanic and Atmospheric Administration
NSWE	Nonlinear shallow water equation
N-S	Navier-Stokes
PNG	Papua New Guinea
Q	Probability of exceedance
r	Random number ranging from 0 to 1
s	Slide center of mass motion, function of time
s_o	Characteristic length of motion
S_f, S'_f	Shape function of slide sides
SMF	Submarine mass failure
S_w	Dimensionless width of disjoined slide pieces
SWE	Shallow water equation
t	Time
t_o	Characteristic time scale of motion
ts	Star motion time of fragmented slide piece

ts'	Dimensionless start motion time of disjoined slide piece
t_Ω	Difference in start motion times between a slide piece and its companion pieces
u_c	Evolving velocity of slide as it moves down slope, function of time
T_{Hmax}	Period of the maximum wave height
u_t	Terminal velocity of slide
U^I	Horizontal water particle velocity at undisturbed water level
V	Volume of submerged slide
VOF	Volume of fluid
w	Wave angular frequency, units of radians
x_l, x_r	Left and right *tanh* inflection points delimiting slide width, functions of time
x_c, x'_c	Horizontal location of slide centre point, function of time
x_o	Horizontal location of slide centre point at rest
xoI	Offshore initial centre point horizontal location of slide
Δt	Numerical time step
$\Delta x, \Delta y$	Numerical space steps
α	Slope angle, units of degrees
γ	Specific gravity of slide (ρ_b/ρ_w)
η	Free surface elevation, function of space and time
θ	Wave angle of approach normal to boundary, in radians
∇_h	Horizontal gradient operator

ρ_b	Bulk density
ρ_w	Water density
ϕ	Fluid velocity potential
φ	Fluid velocity potential at undisturbed water surface level
Ω	Combined space-time coherency of slide, dimensionless
Ω'	Auxiliary variable for numerical computation of Ω
m_m	Combined mass of slide fragments
m_R	Ratio of parent slide mass to mass of slide pieces (m_s/m_m)
m_s	Mass of parent slide

TABLE OF CONTENTS

LIST OF FIGURES

LIST OF TABLES

CHAPTER I

INTRODUCTION AND

CASE STUDY

A tsunami is a series of waves characterized by both extremely long wavelength and period that result from impulsive geological events involving a large body of water, more commonly the ocean, such as earthquakes, volcanic eruptions, aerial and submarine landslides, and meteorite impacts. Tsunami propagation speed, transoceanic travel potential, and attainable height, among other factors, classify these waves as a major hazard to coastal communities around the globe. Throughout history, tsunamis have struck coasts worldwide, many times inadvertently, bringing severe infrastructure, economic, and social damage to the affected areas. The National Geophysical Data Center / World Data Center (NGDC/WDC), a partner of the National Oceanic and Atmospheric Administration (NOAA), documents in the form of a Historical Tsunami Database over 2400 tsunami events dating back to 2000 B.C., listing as causes of these phenomena the geological mechanisms previously mentioned acting either individually or collectively. In recent times, episodes such as the 2004 Indonesia tsunami and the 2011 Japan tsunami, associated to human death tolls in the order of 200,000 and 15,000, respectively, have fostered the development of more robust tsunami hydrodynamic models and more efficient warning systems that can aid in protecting coastal communities, nearshore infrastructure, and the local environment. Both of these events reinstated the importance of reinforcing vulnerable shorelines and educating the people that live in close proximity to the coast about evacuation measures. Though catastrophic tsunamis are infrequent events, the hallmark of their passage may never be entirely erased.

_____

This thesis follows the style of the *Journal of Waterway, Port, Coastal, and Ocean Engineering*.

Although the events in Japan and Indonesia were a consequence of seismic activity, tsunamis may also surge from other mechanisms. Among them, submarine mass failures (SMFs) consist of volumes of seafloor material that, driven by gravity and other body forces, experience motion along a rupture surface. The forcing that provokes a SMF may come from different sources; however, earthquakes have been the most investigated and documented triggering mechanisms. Once set in motion, SMFs stimulate the ocean surface, generating waves of destructible height that can severely damage the coast and offshore assets. For this reason, SMFs are categorized as tsunamigenic mechanisms and potential hazards for civilizations settled along the coast.

Contemplated in the NGDC/WDC Historical Tsunami Database, submarine landslides are a category of SMFs characterized by a rigid body-type motion of essentially no internal deformation. Depending on the rupture surface over which failure of their mass occurs, submarine landslides can be classified as translational or rotational. Translational slides undergo motion over a roughly planar rupture surface whereas rotational slides or slumps experience motion on curved surfaces that exert rotational movement on the failed material. Nonetheless, additional classifications of SMFs (e.g., debris flows, mass flows, and turbidity currents) are derived based on the disintegration, deformation and dilution that slide materials undergo as failure takes place (Lee et al. 2002).

Although not well understood and studied in the past compared to seismic sources, submarine landslides earned their recognition as tsunami-triggering mechanisms as the extent of coastal damage and the number of human deaths were valued in the aftermath of various historical episodes involving this class of SMFs. Some of these events (1888 Trondheim Bay, Norway; 1918 Mona Passage, Puerto Rico; 1929 Grand Banks, Canada; 1958 Lituya Bay and 1964 Resurrection Bay, Alaska; 1998 Sissano Lagoon, Papua New Guinea (PNG); 1999 Fatu Hiva Island, French Polynesia), were driven by natural forcing, while others (1994 Skagway Harbor, Alaska; 1979 Nice Event, France) were a consequence of nearshore construction and harbor/port structural instability.

The 1998 PNG Tsunami: A New Conception of SMFs

Among the memorable recorded events belonging to the underwater landslide category, the tsunami of July 17, 1998, Sissano Lagoon, Papua New Guinea stands out for the number of lives it inadvertently claimed and the importance it had to the research and coastal communities in recognizing the hazard posed by SMFs. The triggered waves of this event, occasioned by a seismically-induced slump, reached up to 10 m in height and devastated 23 km of coast, causing the deaths of over 2200 inhabitants. Within the historical records, the latter death toll makes the 1998 PNG event the worst catastrophe provoked by a tsunami of submarine landslide origin (NGDC/WDC).

In the aftermath of the PNG tragedy, survey teams noticed a tsunami landmark unequal to the more familiar signature of tsunamis solely triggered by earthquakes. The first sign of abnormality was the lack of agreement between the magnitude of the earthquake and the height of the tsunami. Field measurements on the coast indicated that the generated waves exceeded the expected height for a magnitude 7 earthquake, using as reference previous coseismic tsunami events. In addition, the arrival time of the tsunami was not in accord with the occurrence of the earthquake's main shock as reported by eye witnesses who approximated a 20-minute delay between these two events. The earthquake and the tsunami appeared not to share the same geographical origin. Adding to the signs of inconsistency, damage on the coast did not reflect the relatively uniform profile characteristic of a coseismic tsunami. Rather, land surveys indicated that 15 km away from the location of maximum run-up waves were significantly smaller and only minor coast deterioration could be appreciated. The height of the tsunami, its arrival time, and its localized devastation pattern along the coast suggested a different triggering mechanism.

Supporting the hypothesis of a few scientists, marine surveys were able to locate a sign of recent displacement in the ocean floor off Sissano Lagoon. Combined with hydroacoustic data, this finding provided crucial support to the postulate of a submarine landslide-induced tsunami. Further investigation concluded that, provoked by a

secondary aftershock that occurred 13 minutes after the main tectonic disturbance, a volume of 4 km^3 of seafloor material located 35 km offshore of Sissano Lagoon was set in motion for about 45 seconds. Using these data as inputs, numerical models of the affected area were able to reproduce the main characteristics of the tsunami witnessed on July 17, 1998 in the PNG coast. More details of the event can be found in the work of Borrero et al. (2002), Synolakis et al. (2002) and Lynett et al. (2003) from which this narrative was composed.

Though in a lamentable manner, the outcome of the PNG catastrophe gave the devastation potential of submarine landslide tsunamis a new meaning, rectified the need to more deeply study the nature of these events, and motivated the effort to incorporate the hazard posed by SMFs into inundation maps, nearshore evacuation plans and coastal infrastructure design.

CHAPTER II

CHARACTERIZATION OF SUBMARINE

LANDSLIDE-GENERATED TSUNAMIS

It is possible to qualitatively characterize underwater landslide-induced tsunamis and differentiate their features from tsunamis of seismic origin, based on the observations gathered in the wake of past events. It is important to examine the peculiarities inherent to these waves to better understand the coupling between the motion of the ground and the surface of the ocean. This examination will not only allow to identify wave and run-up features, but also the prediction and modeling challenges unique to submarine landslide tsunamis. In general, however, the properties of these tsunamis cannot be quantitatively standardized and are a function of slide dynamics, slide physical properties, and local bathymetry.

Distinction from Tsunamis of Seismic Origin

Compared to coseismic tsunamis, the spatial source extent of a submarine landslide tsunami is much smaller. Consequently, the latter waves manifest peaked wave forms and highly directional propagation patterns that are correlated to the volume and direction of motion of seafloor failure (Iwasaki 1997). Subsequently, these features may result in higher wave amplitudes in the local field, more localized run-up patterns and a greater potential to flood concentrated areas compared to tsunamis triggered by seismic dislocation (Maretzki et al. 2007). Notice these tsunami characteristics are well exemplified by the PNG disaster. In contrast, a relatively uniform wave form and run-up landmark along many kilometers of shoreline is typical of coseismic tsunamis due to the greater source extent which excites the free surface in a more homogeneous manner (e.g., 2011 Japan tsunami).

In contrast to seismic sources, underwater landslides tsunamis are incapable of propagating over transoceanic distances because their energy release is much lower and due to their dispersive nature (Synolakis et al. 2002). Therefore, the hazard of these tsunamis is of primary concern when potential sources rest on shore vicinities. This implies that short arrival times could further aggravate the outcome of tsunamis parented by submarine landslides, as was the case of a vast majority of case studies including the 1998 PNG tsunami.

Prediction and Modeling Challenges

Geotechnical and Geographical Considerations

Several difficulties arise with the study of submarine landslides. An immediate challenge surges from the inability to predict the onset of underwater mass motion, be it due to an external agent (tectonic events, storm-wave loading, low-tide conditions, gas generation from organic matter decomposition, etc.), or to slope instability/over-steepening. Geologists have labeled the areas where submarine mass movements are likely to be encountered, however. Characterized by high environmental loading, these landslide-prone regions correspond to fjords, deltas, submarine canyons, and continental slopes (Lee et al. 2002). Moreover, marine surveys have been able to map the geographical areas where underwater landslides are more likely to occur and to identify very active regions (Booth et al. 2002; Chaytor et al. 2009; McAdoo et al. 2000). In spite of these advances, current remote-sensing technology is not yet able to foresee the failure of these volumes of seafloor material. It is known, however, that excess pore water pressure, liquefaction, deposition rate, critical shear stresses, and local climate are some of the soil-related aspects to consider in attempting to predict or in determining the cause of submarine slope failure initiation (Biscontin et al. 2004; Tappin 2010).

.

Coupling of Submarine Landslide and Free Surface

Comprehending the response of the free surface to the changes occurring in the sea bottom due to the passage of a landslide also poses a major challenge to the study of submarine landslide tsunamis. Compared to earthquakes, the longer time scale of submarine landslides creates a more complex coupling between the changes in the ocean bottom and the free surface. Given the short duration and impulsive nature of the sea floor dislocation in a tectonic event, the initial ocean surface is assumed to mimic the occurred bottom displacement (Jiang and LeBlond 1992). In the case of underwater landslides, the free surface and the moving mass interact for the entire motion duration, generating waves that are a function of the time-history of the ocean bottom changes. If the landslide separates into multiple entities or disintegrates as it travels, then the hydrodynamics involved become even more sophisticated. Furthermore, as was previously mentioned, the extent of an undersea landslide is much smaller than that of a tectonic source. This translates, for the submarine landslide case, into waves of much shorter wavelength (though still in the order of tens of km) that make frequency dispersion in the generation region an important aspect to consider (Lynett and Liu 2002). Therefore, suitable models for the generation and propagation of landslide tsunamis must contemplate the free surface-slide interaction as well as the frequency dispersive behavior of the triggered waves.

CHAPTER III

ANTECEDENT STUDIES AND

PROBLEM STATEMENT

Despite the complexity of the physics involved in submarine landslide tsunamis, multiple analytical solutions and numerical models have been developed and satisfactorily validated against historical and experimental data. In fact, antecedent studies indicate that the problem of submarine landslide tsunamis has been confronted as far back as 1955 with the experimental study of Wiegel who investigated the waves produced by a solid body sliding down a flat slope (Wiegel 1955). Also evident in the literature of underwater landslides is the greater presence of numerical models compared to analytical and experimental studies. The scarcity of the latter two is perhaps the result of the well-established analytical formulations describing flow with ground motion and the high cost of physical experiments able of reproducing submarine slides of variable density that must be meticulously triggered in sufficiently large tanks. As in many other areas of science, numerical models seem to be experiencing significant growth in the topic of submarine landslide tsunamis. Thus, the assortment, theory, and applicability of the existing numerical models will be the main focus of the following literature review.

Numerical and Physical Models with Ground Motion

Three broad categories of numerical models can be identified in the literature: Navier-Stokes (N-S), potential flow, and depth-integrated models. Those that solve the N-S equations form a relatively small, but powerful category. Given that the assumptions of incompressible and irrotational flow are often their only limitations, N-S models are the most robust and accurate means to model the full slide-water surface interaction and the generation, propagation, and run-up of the triggered waves in the presence of currents and nonlinear and dispersive effects. Their potential is illustrated by

models such as the one developed by Assier Rzadkiewicz et al. (1997) that couples sediment and ambient water through the inclusion of rheological terms in the momentum equations and the model of Abadie et al. (2010) which contemplates the air-slide-water interaction that arises in partially submerged slides. Furthermore, N-S models can be equipped with turbulence models (e.g., k-ε and Large-Eddy Simulation) to account for turbulent manifestations such as wave-breaking and large-eddy motions. Liu et al. (2005) and Yuk et al. (2006) incorporated such turbulence models and a Volume of Fluid (VOF) technique (Hirt and Nichols 1981) to study the run-up and rundown occasioned by submarine landslide-induced waves. The accuracy and robustness of N-S models, however, comes at a high computational cost that makes these models inapplicable to large domains.

Though absent of turbulent mixing and wave-current interaction, potential flow models which solve the Laplace Equation are also a way to accurately reproduce submarine landslide-generated tsunamis (e.g., Pelinovsky and Poplavsky 1996) without the need to discard nonlinear and dispersive effects. Most of the potential flow solvers make use of Green's theorem to transform the Laplace Equation into a Boundary Integral Equation (BIE) and reduce the problem dimension by 1 (Lin 2011). For example, Grilli and Watts (1999) developed a two-dimensional (2-D), fully nonlinear BIE model which they solved utilizing a high-order Boundary Element Method (BEM) that is capable of describing the internal flow resulting from underwater landslides. Likewise, Fructus and Grue (2007) designed a three-dimensional (3-D), fully nonlinear, fully dispersive model where the dominant contributions of the integral equations are evaluated using a Fast Fourier Transform (FFT), hence granting remarkable computational efficiency over the model of Grilli and Watts (1999). Nevertheless, potential flow models are complex in essence and fall under the category of computationally expensive models, restricting their applicability to concentrated areas.

By assuming the horizontal scale is much larger than the depth of the fluid or, equivalently, that the vertical velocity of the fluid is small, the N-S equations can be simplified and granted a lower computational cost. This is achieved by integrating the N-

S equations over the water depth and assuming a hydrostatic pressure balance in the fluid. These depth-integrated models are popularly referred to as Shallow Water Equation (SWE) models or long wave models and comprise another widely-used technique for modeling of irrotational flows. In particular, the nonlinear shallow water equation (NSWE) models have been the traditional tool employed to simulate tsunamis of seismic and landslide origin. Jiang and LeBlond (1992, 1993) conducted the first set of numerical investigations of the coupling of a submarine mudslide and the free surface using a NSWE model modified to incorporate ground motion. Similarly, Hienrich et al. (2001) utilized a 2-D NSWE model to recreate the 1998 PNG Tsunami under two scenarios: a slump that behaves as a viscous fluid and a slump that fails in the form of granular material. Conversely, relying on the linear SWE, Raney and Butler (1976) studied landslide-generated waves in a reservoir, Harbitz (1992) and Harbitz et al. (1993) modeled the Norwegian slides of Storegga and Tafjord, Imamura and Imteaz (1995) modeled two-layer flows using a spectral technique, and Iwasaki (1997) established distinctions with regard to wave form and directivity between coseismic and landslide tsunamis. Both linear and nonlinear SWE models, however, are deprived of dispersion terms and limited to regions shoreward from the surf zone (Brocchini and Dodd 2008). These weaknesses reduce the precision with which the SWEs can model submarine landslide tsunamis where frequency dispersion in the generation zone may be relevant and wave propagation into deep water may be a subject of interest.

The introduction of low-order nonlinear and frequency dispersion effects into the SWEs yields another class of depth-integrated models known as Boussinesq models which emerge from the work of Peregrine (1967). The inclusion of dispersive terms allows these models to extend the validity of the NSWE into deeper water and account for diffraction, refraction, shoaling, and reflection effects. Lynett and Liu (2002) modeled a one dimensional (1-D) submarine slide by means of a weakly nonlinear, weakly dispersive Boussinesq model and concluded that, though nonlinear effects are relevant to predict shoreline movement and wave breaking, frequency dispersion is important in the generation region. Extending their Boussinesq model to a 2-D

multilayer scheme, Lynett and Liu (2005) studied the dependency of the run-up generated by 3-D submarine and subaerial landslides on various slide parameters (such as thickness, specific gravity, and beach slope) and estimated the magnitude and location of maximum and secondary run-up peaks. Further exemplifying the potential of these extended depth-integrated models, Fuhrman and Madsen (2009) created a high-order Boussinesq model capable of reenacting moving seafloors (including submarine landslides) and accurately reproducing tsunami generation, propagation, and run-up. As may be speculated, the more inclusive the nonlinear and dispersion effects, the more complex and computationally expensive these Boussinesq models become. This is the greatest limitation of these extended depth-integrated models in addition to their inherent irrotational and inviscid fluid assumptions.

With the purpose of studying detailed wave field characteristics and validating the aforementioned numerical models, laboratory experiments have also been conducted in a variety of set-ups, slide shapes and kinematics, and triggering devices. Although most of these studies have been 2-D reenactments of submarine slides of rigid type (Wiegel 1955; Iwasaki 1982; Heinrich 1992; Watts 1998, 2000; Watts et al. 2000; Grilli and Watts 2005) and granular material (Watts and Grilli 2003; Fritz et al. 2004), 3-D experiments have also been performed for rigid bodies (Synolakis and Raichlen 2003; Enet et al. 2003; Liu et al. 2005; Enet and Grilli 2005, 2007; Cecioni and Bellotti 2010b). Independently, each one of these experiments confirmed the dispersive and directional nature of the wave field created by the motion of underwater slides.

A Source Term Suitable for Submarine Landslides

In light of the dispersive behavior of tsunamis induced by underwater landslides, Tinti et al. (2006) developed a Lagrangian analytical model that incorporates seafloor deformations characteristic of submarine landslides and the frequency filtering effects caused by the water column. In their model, seafloor alterations are incorporated through a forcing function defined as the time derivative of the water depth (h_t) while filtering of

high wave frequencies is implemented by means of a filter function of the form $ff_L =$ sech $(k_s h)$ with $k_s = 2\pi/L_s$ where k_s is the landslide wave number, L_s the characteristic landslide length, and h the local ocean depth. The purpose of the latter function is to act as a low-pass frequency filter and favor the reproduction of long waves. The absence of the filter function would suggest that bottom disturbances are purely transmitted to the free surface. As mentioned previously, however, the time-scale of submarine landslides makes it incorrect to assume that the changes in the ocean bottom instantaneously transfer to the free surface, though it is a valid assumption for coseismic tsunamis. The product of the forcing and filtering functions constitutes the source term of Tinti et al. (2006) which was utilized to simulate the landslide tsunami that struck the island of Stromboli, Italy on December 30, 2002.

Similarly, but following more closely the discussion of Ward (2001), Kervella et al. (2007) stress upon the importance of incorporating frequency-dispersion capabilities to submarine landslide tsunami models. They support this postulate by comparing 3-D linear and nonlinear tsunami generation models that do and do not account for frequency dispersion. Their approach with respect to the linear models is based on two crucial features of Ward's work: the use of a spectral technique to solve the governing equation and boundary conditions and the utilization of wave number (k), rather than k_s, in the formulation of the filter function, i.e., $ff_W =$ sech (kh). Kervella et al. (2007) concluded their study by stating that NSWE models are not able to reproduce the frequency dispersive behavior of tsunamis, but that linear theory inclusive of dispersive manifestations is more appropriate in this regard.

A synopsis of the mentioned studies and their findings suggests that a model for the study of submarine-landslide tsunamis could be formulated using linear theory, but would have to account for frequency dispersion effects in the generation region, grant acceptable accuracy, and be applicable to large domains. To a large extent, these criteria can be satisfied with a model governed by the Mild-Slope Equation (MSE).

The Fully Dispersive MSE Model

Similar to the approach employed to reduce the computational cost of the N-S equations, Mild-Slope Equation models offer a simpler alternative to potential flow models. Proposed by Eckart in 1952 and derived by Berkhoff in 1972, the MSE is a depth-integrated version of the Laplace equation operating under the assumption of inviscid flow and mildly-varying bottom slopes. The "mild-slope" acronym surges from assuming that, within a wavelength, the rate of change in depth is small (Demirbilek and Panchang 1998). Regarding their functionality, MSE models offer a mixture of the benefits and limitations of the SWE and Boussinesq models. Most commonly found in their linear form, MSE models are able to simulate small-amplitude wave environments where wave propagation from deep to shallow water and wave scattering effects (i.e., refraction, reflection, and diffraction) are encountered. The main advantages of an MSE model over Boussinesq approximations is that the former covers a wider range of water depths due to its natural incorporation of frequency dispersion and requires less computational effort. In view of these attributes, the MSE has been embraced as a suitable tool for describing coastal wave climate and wave fields in the vicinity of coastal structures and islands (Demirbilek and Panchang 1998). In particular, owed to its inclusion of frequency dispersion, MSE models are suitable for the simulation of submarine landslide tsunamis.

By incorporating ground motion, Bellotti et al. (2008) developed a linear MSE model capable of reproducing small-amplitude transient waves and frequency dispersion effects caused by changes in the ocean bottom. The forcing function of their model consists of the h_t term, as proposed by Tinti et al. (2006). Regarding the solution approach to their MSE model, Bellotti et al. (2008) adopt the technique of Kervella et al. (2007) who solve their mathematical problem in the frequency domain by means of a Fourier Transform. To validate their model, Bellotti et al. (2008) recreate the propagation of the December 30, 2002 Stromboli tsunami, obtaining results congruent

with the findings of Tinti et al. (2006) and clearly showing the reproduction of frequency dispersion effects when comparing their solutions to those of a long wave model.

Refining the suitability of the linear MSE model of Bellotti et al. (2008) to recreate tsunamis originated by underwater landslides, Cecioni and Bellotti (2010a) incorporated the low-pass filtering influence of the water column into the structure of the source term. Their filter function is the one investigated by Tinti et al. (2006), but with the modification suggested by Kervella et al. (2007) with respect to using wavelength rather than landslide characteristic length. Hence, the source term of their model in the physical space is formed by the product of ff_W and h_t. A Fourier Transform is then applied to obtain the elliptic MSE which will be discussed in the next chapter.

Cecioni & Bellotti (2010a) proceeded to demonstrate the improvements made to the MSE model of Bellotti et al. (2008) by comparing free surface elevations against a 3-D Laplace equation solver. In addition to exposing its computational efficiency, the outcome of this comparison validated the solution accuracy of the MSE model, which turned out to be comparable to that of a Boussinesq equation. At the same time, the satisfactory results were suggestive that the filter function proposed by Kervella et al. (2007) was the appropriate means to recreate the low-pass filtering character of the water column. Among their concluding remarks, Cecioni and Bellotti (2010a) motivated the use of the fully dispersive MSE model in early tsunami warning systems.

Probabilistic Studies on U.S. Coasts

The study of submarine-landslide generated tsunamis lies among the many areas of research where probabilistic methods are often applied. Particularly, the hazard assessment of these waves has been investigated under the Monte Carlo approach as this technique has proven to be suitable for analyzing the behavior of a system that transforms or evolves depending on the random behavior of multiple parameters. The outcome of probabilistic studies of this nature has given valuable insight on the correlation between tsunami amplitudes and slide characteristics (Watts 2004) and has

allowed for the identification of specific sites with high risks of flooding along continental margins (Maretzki et al. 2006; Grilli et al. 2009).

Watts (2004) made use of a BEM (Grilli and Watts 1999) and a Monte Carlo approach to construct tsunami amplitude probability distributions for Southern California in the context of underwater landslides and slumps mobilized by seismic forcing. The various random input parameters defined in his study account for earthquake magnitude ($4.4 < M_w < 7.4$) and distance, sediment characteristics and slide/slump dimensions and are arbitrarily given uniform and Poisson probability distributions. The correlation analysis conducted by Watts (2004) indicates that tsunami amplitude is most strongly dependent on the thickness and length of the submerged mass for both slides and slumps. However, the results of the Monte Carlo simulations suggested that slumps have a greater tsunamigenic potential than slides given their larger width to length ratio. Watts (2004) concluded his study recognizing the challenge of generating precise tsunami amplitude distributions given the lack of tsunami and geotechnical data in the region of the study and the unrealistic parameter combinations that may arise from the Monte Carlo method. In spite of this, he recalls the importance of probabilistically creating tsunami amplitude curves on which both hazard and risk assessment can be promoted.

Similar in methodology to the work of Watts (2004), Maretzki et al. (2006) conducted a probabilistic study, founded on a Monte Carlo method and a long wave model, to determine the tsunami hazard posed by SMFs originated as a result of earthquakes on the continental shelf and slope of the upper U.S. East Coast. Their probabilistic model consists of randomizing input parameters representing seismicity, sediment features, and slide/slump physical attributes to obtain run-up heights associated to 100-year and 500-year seismic return periods. Maximum run-up along the shore is estimated on the basis of the correspondence principle stated by Watts et al. (2005) which approximates maximum run-up to the magnitude of the initial tsunami depression provoked by a SMF. Maretzki et al. (2006) finalize their investigation identifying only two locations along the examined geographical domain (one near Long Island, NY and

another one in the proximity of Atlantic City, New Jersey) with high risk of tsunami-induced run-up topping the regional 100-year storm surge of 5 m. In the concluding remarks, they also stress upon the importance of having actual geotechnical data to better quantify SMF-tsunami hazard.

Elaborating on the work of Maretzki et al. (2006) for the same region, a Monte Carlo-based stochastic study of refined peak horizontal acceleration and slope stability calculations as well as inclusive of nearshore wave breaking and excess pore water pressure was performed by Grilli et al. (2009). In addition, the latter authors impose a 0.02-m threshold for the initial height of the generated tsunamis to proceed with propagation and run-up estimation. Input parameter distributions and initial run-up estimation, however, resemble those of Maretzki et al. (2006), except that along-shore run-up is modulated assuming a Gaussian shape. The risk assessment presented by Grilli et al. (2009) is in terms of run-up heights for given return periods, with an emphasis on the 100-year and 500-year cases. Consequently, the same two sites identified by Maretzki et al. (2006) are again recognized as the most vulnerable locations to SMF-induced run-up. Grilli et al. (2009) concluded their discussion noting the improvement of run-up prediction with the addition of wave breaking and cataloguing the overall coastal hazard for the entire area of the study as low.

Several issues in assessing the hazard presented by submarine landslides and slumps can be inferred from the aforementioned probabilistic studies. First, actual bathymetry and sediment data are of primary importance to model the generation and propagation of the generated tsunamis. Although bathymetry seemed to be readily available, all three studies recognized the need to better sample continental margins to reduce the uncertainty in the distribution of input sediment parameters. Second, these studies also reflect the challenge in associating precise SMF tsunami risk levels to specific areas, given the simplifying assumptions and the impractical combinations that may result from the Monte Carlo method.

The studies of Watts (2004), Maretzki et al. (2006) and Grilli et al. (2009) are outstanding examples of the valuable insight that can be gained through the use of

Monte Carlo simulations to estimate the hazard posed by submarine landslide tsunamis. These investigations, however, only explored failures that occur as a single moving entity, thus not providing insight on the hazard potential of submarine landslides that may break into multiple pieces as failure unfolds. It is this gap in the probabilistic studies of SMFs which will be addressed and to a first-order of approximation quantified in this study.

Objective and Methodology of the Study

By numerically recreating the linear MSE model of Cecioni and Bellotti (2010a) using a finite-difference scheme, this research aims at probabilistically analyzing the shoreward-traveling waves generated by 1-D submarine rigid landslides that experience translational failure. Deviating from the failure modes found in the literature, the modeled landslides possess the capability to fail either as a single rigid mass or as a user-specified number of rigid pieces. For the latter case, an expression for the space-time coherency of the landslide will be presented in order to conceive the degree of compaction of the overall failure. As inputs to the model, eight dimensionless slide parameters influencing tsunami generation will be considered, namely: bottom slope, slide width, slide initial depth, number of pieces in which the slide detaches, slide failure delay, and specific gravity, drag coefficient, and added-mass coefficient of the slide mass. The latter three inputs will be randomly selected using normal distributions while the rest will be deterministically chosen and organized in the form of a parameter space.

To evaluate the free surface response to the various parameter combinations, Monte Carlo simulations will be used to obtain probability of exceedance curves for the maximum dimensionless wave height from which wave statistics will be extracted. In addition, nondimensional relations between wave period and maximum wave height will also be provided. The results of the Monte Carlo simulations will then be presented for a parameter subspace with constant values and a parameter space in which one of the inputs is singularly varied. Tsunami hazard assessment will then advanced by providing

insight on the dependency of tsunami generation on the different slide parameters and by providing first-order estimation for nearshore design of the height of the waves that may be triggered by underwater landslides. Landslide triggering, wave breaking and run-up are beyond the capabilities of the recreated model; hence, the present study is limited to wave generation and propagation.

The rest of this manuscript is organized in the following manner. The next section introduces the governing equations and boundary conditions of the MSE model. Then, recreation and validation of the 1-D and 2-D models are covered along with the equations of motion governing slide dynamics. Next, the Monte Carlo simulations are addressed in terms of their organization, numerical setup, and selection of deterministic and random inputs. The interpretation of the resulting probability distributions is then overseen as well as the inspection of the degree of influence of the different slide parameters on tsunami generation. Finally, conclusions are drawn and future developments suggested.

CHAPTER IV

NUMERICAL RECREATION AND VALIDATION

OF A LINEAR MSE MODEL

Aware of the potential of the MSE and of the relevance of frequency dispersion in tsunami theory, Bellotti et al. (2008) construct a mathematical model centered about the frequency-dependent linear MSE which they justifiably modify to incorporate the seafloor alterations characteristic of earthquakes and underwater landslides. To arrive to this equation, Bellotti et al. (2008) follow the derivation of the hyperbolic or time-dependent MSE proposed by Dingemans (1997) and proceed to apply a spectral method which, by means of a Fourier Transform in time, yields the final form of the elliptic MSE. The time-domain solution is then recovered through an Inverse Fourier Transform.

Mathematical MSE Postulate

The start point of the MSE derivation is the 2-D set of linearized wave equations for incompressible and irrotational fluid on an uneven bottom, namely

$$\nabla_h^2 \phi + \phi_{zz} = 0 \qquad -h(x,y,t) < z < 0 \tag{1}$$

$$\phi_z + \frac{1}{g} \phi_{tt} = 0 \qquad\qquad z = 0 \tag{2}$$

$$\phi_z + \nabla_h \phi \cdot \nabla_h h = 0 \qquad\qquad z = -h(\text{x,y,t}) \tag{3}$$

where $\phi(x, y, z, t)$ is the velocity potential in the fluid, $h(x, y, t)$ is the water depth, g is the gravitational acceleration and $z = 0$ the location of the undisturbed water surface. The symbol ∇_h is the horizontal differential operator denoting divergence in the x and y directions. Equation (1) is the Laplace Equation, Equation (2) is the combined dynamic

and kinematic free surface boundary condition, and Equation (3) is the impermeable bottom boundary condition.

The solution to the boundary value problem posed by Equations (1) - (3) is assumed to be of the form

$$\phi = f(z, h)\varphi(x, y, t) \tag{4}$$

where φ (x, y, t) is the velocity potential at the undisturbed water surface and $f(z, h)$ is a function that approximates the variation of the kinematic field with depth along the water column. From linear theory, f is chosen as follows

$$f = \frac{cosh[k(h+z)]}{cosh\,(kh)} \tag{5}$$

where k is the wave number. Equation (5), although valid for harmonic waves propagating over an even bottom, holds for slowly-varying bottoms as well. Wave number can be computed for any angular frequency w through iteration of the linear dispersion relationship, i.e.,

$$w^2 = gktanh(kh) \tag{6}$$

Alternatively, wave number can be calculated by using Eckart's approximation to the linear dispersion relationship (Fenton and McKee 1990). This accurate approximation suppresses the need to iterate for k by taking the following form

$$k = \frac{w}{g}\left[coth\left(\frac{w^2h}{g}\right)\right] \tag{7}$$

Governing Equation

By means of a variational derivative originated from Hamiltonian theory of surface waves, Dingemans (1997) constructs two evolution equations for the free surface elevation η and the velocity potential at $z = 0$. These equations are

$$\eta_t = G\varphi - \nabla \cdot (F\nabla\varphi) - h_t \tag{8}$$

$$\varphi_t = -g\eta \tag{9}$$

where, in Equation (8), h_t is the heuristically-added term responsible for incorporating any seafloor alterations occurring as a result of earthquakes or submarine landslides. Also present in Equation (8) are the variables F and G which are defined as follows

$$F = \int_{-h}^{0} f^2 dz = \frac{c\, cg}{g} \tag{10}$$

$$G = \int_{-h}^{0} \left(\frac{\partial f}{\partial z}\right)^2 dz = \frac{w^2 - k^2 ccg}{g} \tag{11}$$

where c is wave celerity and cg is group velocity. By differentiating Equation (8) with respect to time, it is possible to remove the variable φ from the first evolution equation with the aid of the equality established in Equation (9). After this simplifying procedure, the following second-order partial differential equation results

$$\eta_{tt} - \nabla \cdot (gF\nabla\eta) + gG\eta = -h_{tt} \tag{12}$$

This equation of hyperbolic nature is referred to as the time-dependent MSE and is capable of reproducing the propagation of waves with a narrow frequency band. In view of this limitation, Bellotti et al. (2008) use a spectral method on Equation (12) to amplify its wave spectrum, hence increasing its adequacy for tsunami simulation. The

spectral technique consists of performing a Fourier transformation with respect to time to each term of the hyperbolic MSE. Carrying such transformation, substituting the expressions for *F* and *G*, and doing some algebraic manipulation yields the elliptic, frequency-dependent MSE, namely

$$\nabla \cdot (ccg\nabla N) + w^2 \frac{cg}{c} N = h_F \tag{13}$$

where $N(x, y, w)$ and $h_F(x, y, w)$ are the Fourier Transform of $\eta(x, y, t)$ and $h(x, y, t)$, respectively. Equation (13) is widely utilized to model small amplitude surface gravity waves in coastal regions (Demirbilek and Panchang 1998). Now in the frequency domain, Equation (13) is to be solved for each wave frequency in a specified frequency range. The time-domain solution is recovered by taking the inverse Fourier Transform of $N(x, y, w)$ to regain $\eta(x, y, t)$. The free surface elevation due to ground motion can then be evaluated. Equation (13) may be further simplified by assuming shallow water limits or that $c = cg$.

More importantly, the elliptic MSE can be adapted to more closely reenact the physics involved in underwater mass failures. On the reasoning grounds of Tinti et al. (2006) and Kervella et al. (2007), Cecioni and Bellotti (2010a) propose the addition of a filter function to the source term on the right-hand side of Equation (13) to reproduce the low-pass filter effect of the water column. Finally, the elliptic MSE equipped to model tsunamis with submarine landslides as their forcing mechanism is of the form:

$$\nabla \cdot (ccg\nabla N) + w^2 \frac{cg}{c} N = (ff_w) h_F \tag{14}$$

where $ff_W = \text{sech } (kh_o)$ and h_o denotes, on the basis of small-thickness landslides, the bottom depth in the absence of the landslide. Cecioni & Bellotti (2010b) present a different derivation of Equation (14) by incorporating the wave-generating source term h_t into Equation (3), the bottom boundary condition. Nevertheless, they utilize the same spectral technique described here and arrive to the same governing equation.

Furthermore, Cecioni and Bellotti (2010a,b) have conducted various numerical experiments and one 3-D laboratory experiment demonstrating the validity of the solutions provided by Equation (14) and the computational benefits of the linear MSE model when compared to other models of higher accuracy and more expensive computational cost. In light of their validation work, the solutions provided by Equation (14) are considered, for the purpose of this research, appropriate for modeling small-amplitude waves of underwater landslide origin.

Boundary Conditions

As indicated by Bellotti *et al.* (2008), Equation (14) may be assigned three types of Neumann lateral boundary conditions. The first type corresponds to a fully reflective condition appropriate for solid boundaries

$$N_\mathrm{n} = 0 \tag{15}$$

where the subscript *n* denotes the outgoing vector normal to the boundary. On the contrary, a radiation condition that allows the waves to exit the computational domain can be imposed through the following expression

$$N_\mathrm{n} + \hat{\imath}\,k cos(\theta_n)N = 0 \tag{16}$$

where $\hat{\imath}$ is the unitary imaginary number defined as the $\sqrt{-1}$ and θ_n is the wave approaching angle normal to the boundary. Lastly, a wave-maker condition can also be established on a lateral boundary as follows

$$N_\mathrm{n} = -\frac{iw}{g}U^I \tag{17}$$

where U^I is the horizontal particle velocity at z=0 of the desired wave field normal to the wave-maker boundary. Free surface boundary conditions do not need to be specified for they are inherent in the mathematical formulation of the MSE, as shown in the previous section.

Having formulated the governing equation and boundary conditions, the first phase of this research aims at numerically recreating the described mathematical model in one and two horizontal dimensions. This replica will then need to be validated by comparing free surface elevations against its parent model and other numerical and experimental benchmarks. Upon completion of this phase, the advantages and limitations of utilizing the linear MSE as a vehicle to model submarine-landslide tsunamis will be identified. In the following phases of the present study, the simplicity, accuracy, and computational efficiency of the MSE model will be used to expand on what is known about coastal hazard assessment with regard to submarine landslide tsunamis.

Numerical Recreation of 1-D MSE Model

The numerical approach of Cecioni and Bellotti (2010a) consists of a finite element scheme that approximates the solution to the elliptic MSE subjected to the mentioned boundary conditions. In contrast, the version presented in this study is entirely based on a FTCS finite-difference scheme. By definition, the adopted scheme is first-order accurate in time and second-order accurate in space. Using this approach, the recreated model is entirely coded in MATLAB 7.6.0. For the 1-D problem, a tri-diagonal matrix solver based on the Thomas algorithm is used to solve the governing equation (Eq.14) with the appropriate boundary conditions.

The first attempts to create a functional copy of the linear MSE model were based on a 1-D 4-m long, 0.1-m thick slide moving on a flat, horizontal bottom for about 2 s in a 1.0-m water depth. The x-domain was 10-m long and discretized in space steps (Δx) of 0.05 m. The simulation time length was 100 s with time steps (Δt) of 0.1 s. In

addition, the lateral boundaries of the domain were specified as radiation conditions with waves normally leaving the domain, corresponding to θ_x-values of zero on the left boundary and π on the right boundary. This set-up was taken from the 1-D numerical experiments performed by Cecioni and Bellotti (2010a) in the validation phase of their model. Cecioni and Bellotti (2010a) make use of a semi-elliptic landslide which, at a sudden instant, impulsively begins to move with a constant speed for 2 seconds and then comes to absolute rest. Unfortunately, using the landslide geometry and motion of the original model, the recreated model did not produce comparable solutions to those shown in Cecioni and Bellotti (2010a).

As an alternative, the motion of the landslide was chosen to follow a 1-D Gaussian function which was customized to approximate the dynamics of the landslide described in Cecioni and Bellotti (2010a). Due to the nature of the Gaussian function, however, the landslide does not begin motion impulsively, but experiences a smooth acceleration that reaches a peak before deceleration comes into play. Therefore, wave amplitudes were not expected to match those of the parent model, but similarity in magnitude was hoped. To further simplify the recreated model, the semi-elliptic landslide was replaced by a body whose shape was given by a Gaussian function with a fourth-order exponent to flatten the middle section of the bell-shaped curve and obtain a better resemblance to a semi-elliptic geometry. The smoothness of the Gaussian functions permitted the computation of the free surface and the preliminary evaluation of the recreated model. Nevertheless, significant improvement over the first attempt was not observed, which meant that landslide geometry and motion were not the causes of the unsuccessful results.

With the purpose of correcting the recreated model, a 1-D numerical experiment involving a wave-maker boundary condition was performed. This scenario is the simplest provided by Bellotti et al. (2008) because the MSE source term is equal to zero due to the unchanging bottom. On one lateral boundary, the wave-maker condition represented by Equation (17) was specified; on the opposite boundary, a radiation condition (Equation 16) was imposed. A symmetric sinusoidal wave of the specified

height and period propagating over the constant-depth bottom was expected. However, the erratic wave behavior of the first number of trials suggested that the wave frequencies were being calculated in the wrong manner for the rest of the scheme, including the matrix solver, was indisputably well defined. At this point, angular frequencies were being calculated using the time vector (t), i.e., $w = 2* \pi / t$. Therefore, the frequency vector was redefined as the product of the number of time steps (nt) and the frequency resolution (Δf), namely

$$\Delta f = \frac{1}{\Delta t * nt} \tag{18}$$

$$f_q = [0:1:nt-1] * \Delta f \tag{19}$$

where f_q is the temporal frequency in units of hertz. The expression inside the squared brackets in Equation (19) denotes a vector of size nt with elements spanning from zero to nt - 1 in increments of 1. Angular frequencies needed to compute wave number and other quantities are then calculated as follows:

$$w = 2 * \pi * f_q \tag{20}$$

Once this change was implemented, the symmetric sinusoidal wave of constant height was successfully reproduced. In addition to the new approach to calculating angular frequency, the wave-maker model allowed for one more refinement to be made to the recreated MSE model. Given that the input wave height had to be reconstructed after taking the inverse Fourier Transform of the frequency-domain solution, a wave that was different in height from the input height was an indication that a scaling factor was needed. Indeed, a factor of 2 multiplying the solution was found to be required to obtain the proper wave height. The linearity of the model permits the placement of this factor either in the calculation of the source term prior to solving the tri-diagonal matrix or in the recovery of the time-domain solution.

Likewise, the new additions were carried to the Gaussian-shaped landslide model which satisfactorily responded to the implemented changes. Although the difference in landslide shapes created distinct free-surface responses, comparison of results between the parent model's semi-elliptic landslide and the recreated model revealed that maximum surface elevations in the generation area were similar in magnitude. With respect to improving the recreated model, the Gaussian-shaped landslide scheme provided insight in the simulation time length needed to achieve convergence of the solution. Slight variations in the free surface elevations were observed when the time length was increased by 100 s. Though simulation times in the order of 100 s yield acceptable results, time lengths of 500 s were observed to produce converged solutions for Δx and Δt values of 0.05 and 0.1, respectively.

Validation of 1-D Recreated MSE Model

In order to demonstrate the validity of the recreated model, the semi-elliptic landslide model was revisited and modified to resemble the functional scheme of the wave-maker and Gaussian-shaped landslide models. The agreement between the original and recreated model is shown in Fig. 1 which is a combination of the surface time series contained in Figs. 2 and 7 in Cecioni and Bellotti (2010a). To carry out the comparison, the time series of Cecioni and Bellotti (2010a) were digitized using Engauge Digitizer 4.1 and exported to MATLAB. The domain properties are summarized as follows. The domain length in the x-direction is limited to 10 m with $\Delta x = 0.05$ m. The length of the time series was set to 100 s with $\Delta t = 0.1$ s.

In Fig. 1, snapshots (a) and (b) display a time series obtained with a 1-D 4-m long semi-elliptic landslide translating over a flat, horizontal floor. The lateral boundaries of this scenario are specified as radiation conditions (Equation 16). Subplots (c) and (d) show the free surface resulting from the displacement of a 4.21-m long semi-elliptic landslide which moves downwards on a 1:3 slope. For this case, the left boundary, where $x = 0$, is conferred reflective properties (Equation 15) by using a

0.0001-m water depth; the right boundary, where the water depth is at its maximum, is given radiation properties (Equation 16). Moreover, components (a) and (c) of Fig. 1 evaluate the free surface at a horizontal location 1 m away, in the direction of increasing *x*-values, from the landslide centre point at rest. Similarly, Fig. 1(b) and 1(d) represent the surface time series at a location on the horizontal plane 6 m away from the landslide centre point prior to motion.
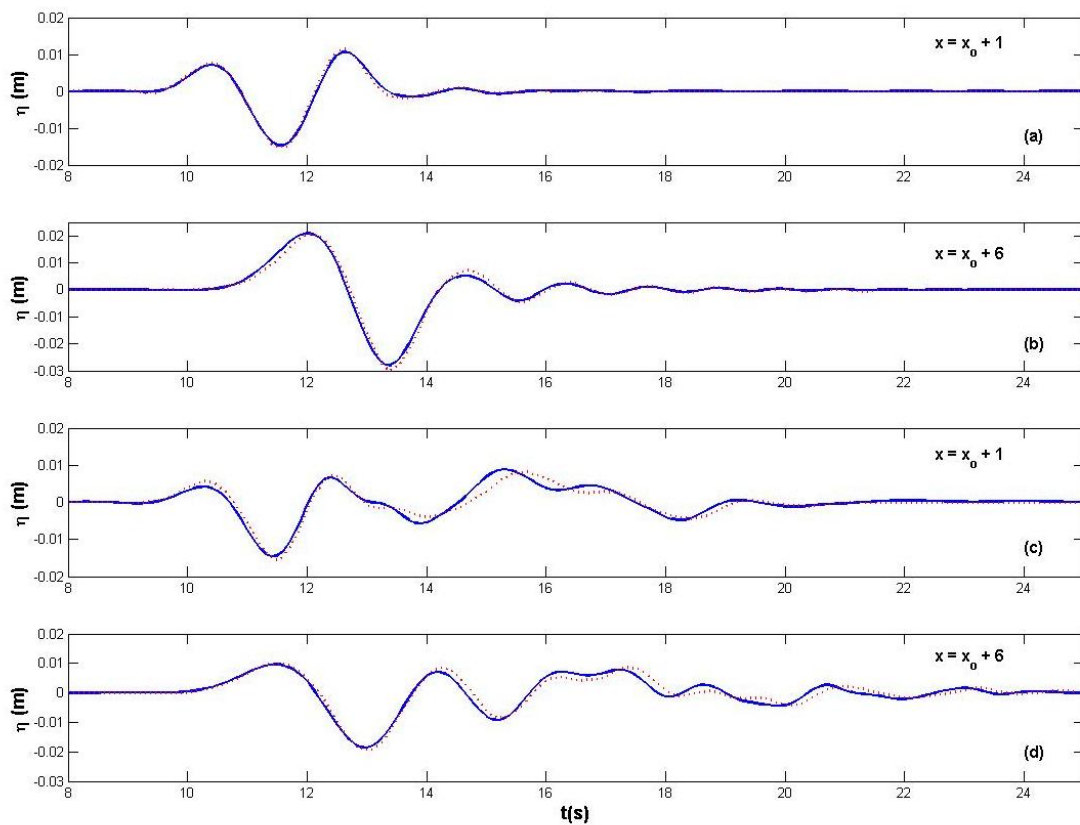
FIG. 1. Free Surface Elevations Computed with the Recreated MSE Model (Solid Line) Compared to the Digitized Time Series of the Original MSE Model (Dotted Line).

Subplots (a) and (b) in Fig. 1 show remarkable agreement with minor wave height underestimation by the recreated MSE model evident in the vicinity of the largest

trough.   Though also revealing satisfactory agreement, subplots (c) and (d) show evidence of a subtle phase lag between the two models near t = 14 s. The moderately accurate process chosen for image digitization may have also influenced the results shown in Fig. 1. In spite of this, good agreement is observed throughout the evolution of the free surface between the two MSE models.

Cecioni and Bellotti (2010a) report a computational time of 7 s and 130 s for the horizontal and sloped bottom scenarios, respectively, on a 2-GHz CPU, 4-GB RAM computer. In addition, they solve Equation (14) for a reduced angular frequency range ($2\pi \cdot 10^2 \leq w \leq 2\pi \cdot 2$) associated to a significant content of wave energy. Computational times recorded with the recreated MSE model for the full range of frequencies ($2\pi \cdot 10^2 \leq w \leq 2\pi \cdot 10$) were found to be 2.4 s for the flat-bottom case and 2.3 s for the sloped-bottom scenario on a 2.49-Ghz CPU, 3.25-GB RAM computer. These computational times lead to the conclusion that the recreated model is not only satisfactorily accurate, but also computationally very efficient with respect to the original version.

Comparison of 1-D Recreated MSE Model against Nonlinear Models

Given the satisfactory performance of the recreated model when compared to its original version, further evaluation was carried out with the purpose of rectifying the accuracy of the MSE duplicate. This time, however, nonlinear models were the reference for comparison. The main purpose of this 1-D evaluation was to examine the importance of nonlinear effects in the evolution of the free surface, particularly in the generation region where the recreated MSE model is desired to be accurate. The selected nonlinear models correspond to the fully nonlinear, weakly dispersive depth-integrated model of Lynett and Liu (2002), the high-order Boussinesq model of Fuhrman and Madsen (2009), and the BIEM which served as reference for comparison for both of these studies. The numerical set-up utilized in this validation process was taken from Lynett and Liu (2002) and is shown in Fig. 2 which illustrates the seafloor conditions and landslide features.
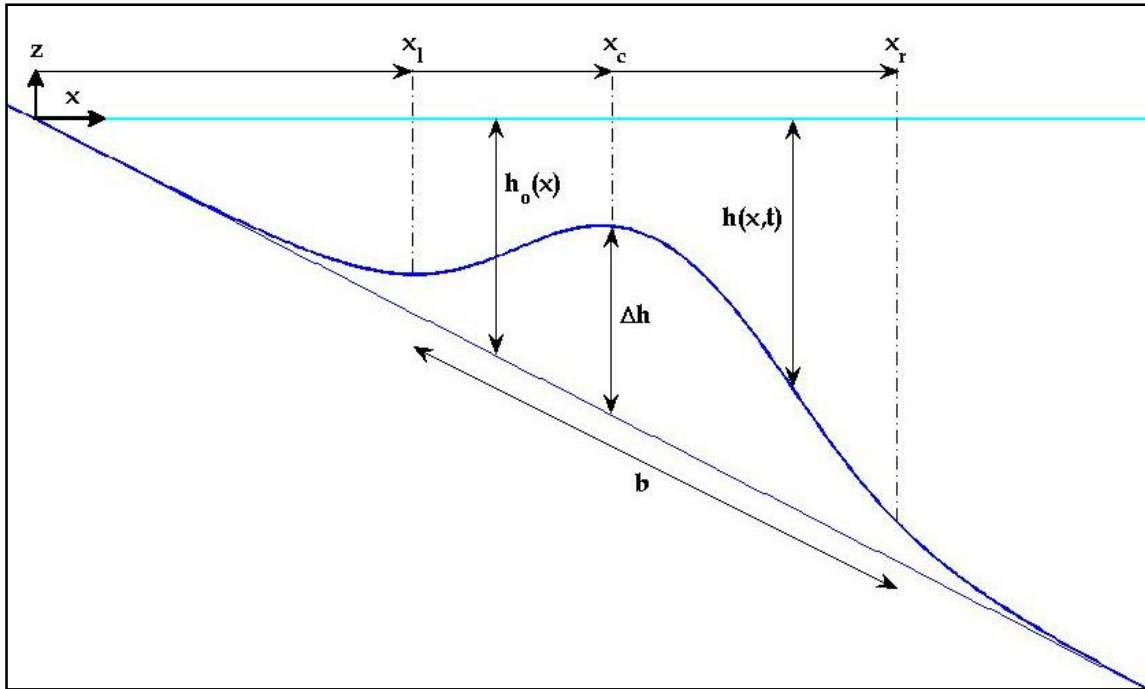
FIG. 2. Submarine Landslide Set-Up for Comparison of 1-D MSE Model Against Various Nonlinear Models.

The physical problem being numerically modeled is that of a smooth body sliding down a plane incline with a coast-resembling boundary opposite to an offshore open boundary. The former boundary is given reflective properties (Equation 15), while the latter is granted radiation capabilities (Equation 16). Before showing the outcome of this comparison, however, the equations that describe the motion of the slide shown in Fig. 2 will be presented. These equations, in fact, will also govern the slide dynamics of the model used for the probabilistic component of this study.

Slide Equations of Motion

The dynamics of the rigid slide depicted in Fig. 2 are dictated by a balance of forces about the slide center of mass involving inertial, frictional, added mass, gravitational, and buoyant forces. Thus, ignoring Coulomb friction effects, the slide

center of mass motion *s(t)* is governed by the following differential equation (Watts 1998)

$$(\rho_b + C_m\rho_W)V\frac{d^2s}{dt^2} = (\rho_b - \rho_W)Vg\sin(\alpha) - \frac{1}{2}C_d\rho_wA\left(\frac{ds}{dt}\right)^2 \tag{21}$$

where ρ_b is the bulk slide density, ρ_w is the water density, C_m is the added-mass coefficient, C_d is the drag coefficient, α is the bottom slope (in degrees), and V and A are the submerged volume and area, respectively, occupied by the slide. At time $t = 0$, it is assumed that $s = 0$, $(ds/dt) = 0$, and $(d^2s/dt^2) = a_o$ where a_o is the slide initial acceleration. Likewise, after a sufficiently long time, a terminal velocity $(ds/dt) = u_t$ is assumed to be reached, meaning $a_o = 0$. Applying these conditions on Equation (21) results in:

$$a_o = \frac{(\gamma-1)g\sin(\alpha)}{\gamma + C_m} \tag{22}$$

$$u_t = \sqrt{\frac{\pi gb(\gamma-1)\sin(\alpha)}{2C_d}} \tag{23}$$

where γ is the slide specific gravity ($\gamma = \rho_b/\rho_w$) and b is the slide width parallel to slope (Fig. 2). The presence of C_m, C_d, and γ in Equations (22) and (23) indicate that shape and sediment characteristics are influential factors in determining the initial acceleration and terminal velocity of the slide. An adequate value for C_m and C_d has been estimated, at high Reynolds numbers, to be equal to 1.0 (Watts 1998, 2000). The solution for s to Equation (21), using Equations (22) and (23), is given by:

$$s = s_o\ln\left[\cosh\left(\frac{t}{t_o}\right)\right] \tag{24}$$

with characteristic length of motion (s_o) and characteristic time scale of motion (t_o) dictated by

$$S_o = \frac{u_t^2}{a_o} \tag{25}$$

$$t_o = \frac{u_t}{a_o} \tag{26}$$

Alternatively, the solution to Equation (21) for slide center of mass velocity (*ds/dt*) takes the following form

$$\frac{ds}{dt} = u_t * tanh\left(\frac{t}{t_o}\right) \tag{27}$$

A more thorough description of the introduced equations for rigid-slide motion is given in Watts (1998). The availability of the set of equations formed by Equations (22) – (26) permits the computation of the water depth function (h_p), as presented in Lynett and Liu (2002), which describes the passage of the 1-D submerged landslide shown in Fig. 2, namely

$$h_p(x,t) = h_o(x) - \frac{1}{4}\Delta h\left\{1 + tanh\left[\frac{x-x_l(t)}{S_f}\right]\right\}\left\{1 - tanh\left[\frac{x-x_r(t)}{S_f}\right]\right\} \tag{28}$$

where Δh is the maximum vertical height of the slide; x_l and x_r are, respectively, the tanh inflection point of the slide left side and right side; and S_f is a steepness factor which acts on the slide sides. Except for the latter, these variables can be geometrically understood by examining Fig. 2. Mathematically, x_l, x_r and S_f are expressed as follows:

$$x_l(t) = x_c(t) - \frac{1}{2}bcos(\alpha) \tag{29}$$

$$x_r(t) = x_c(t) + \frac{1}{2}bcos(\alpha) \tag{30}$$

$$S_f = \frac{0.5}{cos(\alpha)} \tag{31}$$

in which x_c, the location of the slide centre point on the horizontal plane, is given by

$$x_c(t) = x_o + s * cos(\alpha) \tag{32}$$

where x_o is the slide centre point horizontal position at rest. The last four expressions complete the set of equations needed to model the bottom alterations caused by the displacement of an underwater slide through Equation (28). A Fourier Transform is then applied on $h_p(x, t)$ to convert it into the forcing function of the frequency-dependent MSE.

Comparison of Solutions

The evaluation of the recreated MSE model under the explained set-up and equations of motion is shown in Fig. 3. These results correspond to a slide with the following properties: Δh = 0.05 m, b = 1 m, α = 6°, γ = 2.0, C_m = C_d = 1.0, and x_o = 2.379. The numerical domain is 10 m in the x-dimension and uniformly discretized using Δx = 0.05 m. The simulation time length equals 100 s with Δt = 0.01 s for a total of 50,001 time steps.
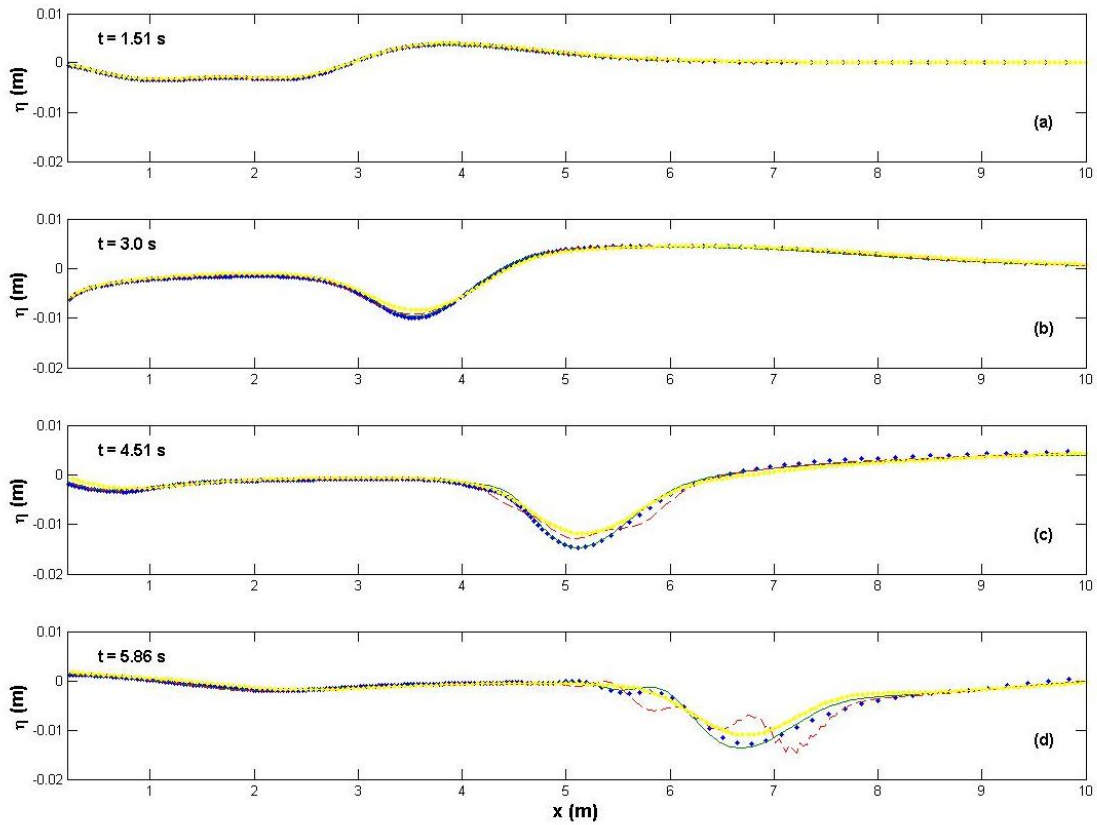
FIG. 3. 1-D Comparison between the Nonlinear, Weakly Dispersive Depth-Integrated Model (Dashed Line) of Lynett and Liu (2002), the High-Order Boussinesq Model (Solid Line) of Fuhrman and Madsen (2009), the BIEM (Dots) as Described in Lynett and Liu (2002), and the Recreated MSE Model (Dotted Solid Line).

Near the generation area (Fig. 3a), excellent agreement is discerned between the various models at all locations within the domain. At $t = 3.0$ s (Fig. 3b), quite good agreement is still observed, though the solution provided by the recreated MSE model slightly undervalues the trough that travels with the slide ($3 < x < 4$). The shoreward-propagating wave, however, is well captured. At a later time, Fig. 3c shows a more pronounced underestimation of the trough above the slide by the recreated MSE model with respect to the BIEM and the high-order Boussinesq model. Contrary to the model of Lynett and Liu (2002), the recreated MSE model appears to remain stable as deeper water is entered due to its fully dispersive character. By the time $t = 5.86$ s is reached

(Fig. 3d), nonlinear effects are more evidently manifesting, which prevents the recreated MSE model from offering a precise match. Nonetheless, the recreated MSE model again demonstrates its full inclusion of dispersion effects by adequately propagating the slide-driven trough into deeper water.

The results shown in Fig. 3 are suggestive that in the generation region, nonlinear effects are of secondary importance and that the recreated MSE model captures the free surface response in the initial failure stages very well. These nonlinear effects, however, do seem to acquire relevance as the slide continues its trajectory down slope. The absence of nonlinearities is, indeed, the most prominent limitation of the recreated MSE model for the order of accuracy of the chosen scheme did not seem to negatively impact the behavior of the solution. In addition, Fig. 3 corroborated the adequacy of the recreated MSE model to simulate wave propagation into deep water. Therefore, given the exemplary agreement in the initial failure stages (Fig. 3a and 3b) and the good reproduction of dispersion effects throughout the free surface evolution, the results shown in Fig. 3 are considered satisfactory and affirm the validity of the 1-D recreated MSE model.

Despite the good performance of the recreated model, an unexpected issue was encountered during this comparison. As the slide leaves the numerical domain, waves of considerable amplitude are consistently reflected off the open right boundary. Attempts were made to correct this behavior by inserting the source term into the radiation condition; however, the reflected waves could not be removed. As will be noticed in the next chapter, this issue had implications of considerable weight.

Evaluation of 2-D Recreated Model

A 2-D version of the numerical experiments covered in this chapter (semi-elliptic landslide, Gaussian-shaped landslide, and the landslide depicted in Fig. 2) was also created. Free surface animations of these scenarios confirmed one of the most peculiar characteristics of submarine landslide-induced tsunamis as noted in field surveys

posterior to the 1998 PNG Tsunami: a peaked wave subjected to rapid lateral decay. More formally, validation of the 2-D MSE replica was carried out by attempting to duplicate the times series displayed in Fig. 14 in Fuhrman and Madsen (2009) corresponding to a laboratory experiment conducted by Enet and Grilli (2007) in which a 3-D rigid slide translates down a 15°-slope. To replicate the 0.082-m thick, 0.395-m wide slide, a 2-D uniform grid of $\Delta x = \Delta y = 0.05$ m was specified to cover a 2-m wide, 3-m long domain. The simulation time length was 250 s with $\Delta t = 0.01$ s for a total of 25001 time steps.

The reference time series (Fig. 14 in Fuhrman and Madsen 2009) were digitized with Engauge Digitizer 4.1 and plotted against the results produced by the recreated MSE model. Fig. 4 shows the agreement of this comparison. For future reference, the x-coordinate of Fig. 14c given in Fuhrman and Madsen (2009) does not actually correspond to the point where the time series is being evaluated. The coordinates of that location should be $(x, y) = (1.929,0)$ as shown in Fig. 4c of this manuscript (Fuhrman, personal communication, 2011).
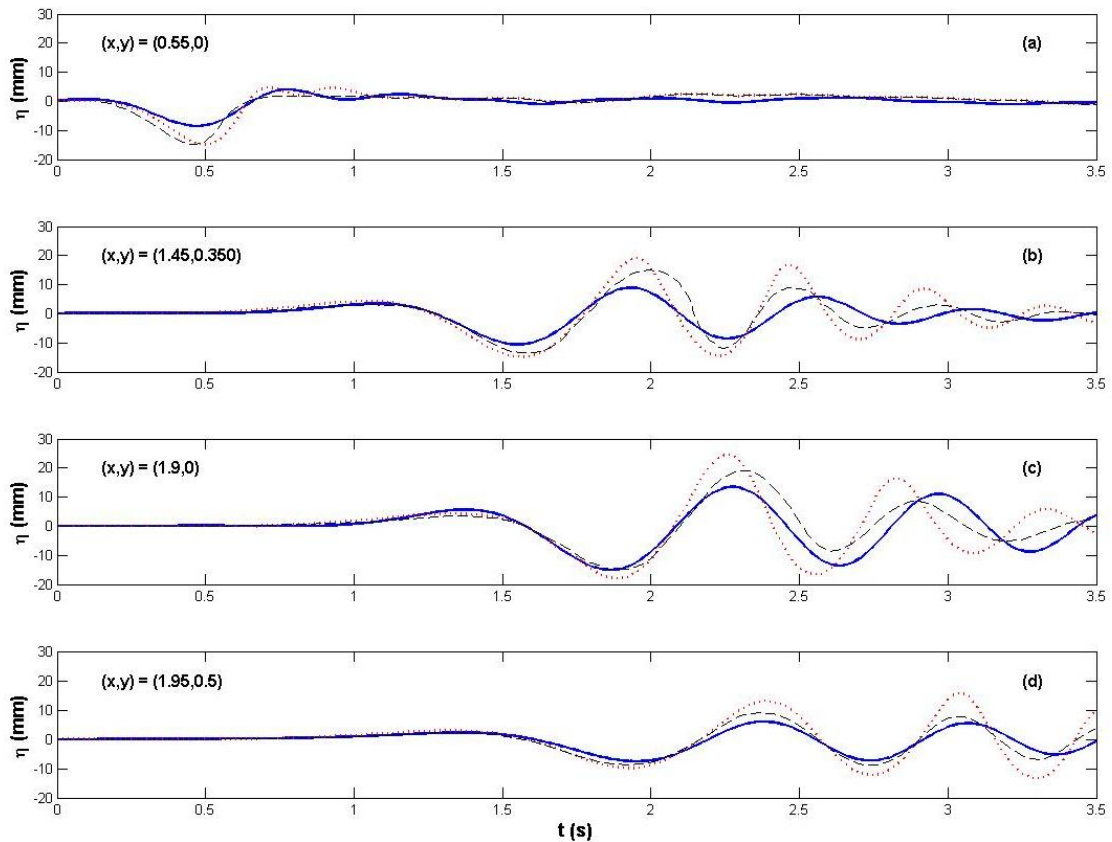
FIG. 4. Evaluation of 2-D Recreated MSE Model (Solid Line) Against the High-Order Boussinesq Model (Dotted Line) of Fuhrman and Madsen (2009) and the 3-D Experiment (Dashed Line) of Enet and Grilli (2007).

Despite the distinct wave theories supporting each model, good agreement is observed in Fig. 4 at the four time-series locations. Similar to the 1-D validation results, the absence of nonlinear effects in the recreated MSE model manifests in the form of wave height discrepancy and phase error. In this comparison, however, the recreated MSE model makes a poor prediction of the free surface behavior in the generation region (Fig. 4a). In spite of this, the inaccuracy seems to diminish as the slide moves away from this region (Figs. 4b - 4d), especially with respect to the experimental results. With regard to the Boussinesq solution, the recreated MSE model is observed to underestimate the wave heights in the dispersive tail and not to consistently capture the

phase of the waves past the leading wave of the dispersive tail. Moreover, the recreated MSE model seems to generate a wave train containing less energy than the one produced by the Boussinesq model in all four time series. In general, Fig. 4 suggests that solution disagreement between the recreated MSE model and the Boussinesq model is more evident for the 2-D case, perhaps indicating that nonlinear and 3-D effects are important. With respect to the experimental data, the recreated MSE model shows a better match in terms of both wave height and phase in the dispersive tails of Figs. 4b – 4d than with the Boussinesq model. All three data sets, however, agree well in the formation of the lead positive wave prior to the development of the spurious tail (Figs. 4b – 4d).

Due to virtual memory constraints, grid resolution could not be refined to match the precise time series locations as given in Fuhrman and Madsen (2009). Rather, the recreated MSE model solutions in Fig. 4 were obtained at the nearest possible computational node from where the gauges of Enet and Grilli (2007) were placed. Sensitivity to the evaluation location of the time series with the recreated MSE model is indeed appreciable, indicating that some improvement of the agreement shown in Fig. 4 should be expected with grid refinement. Nevertheless, further validation would be necessary to safely utilize the recreated MSE model to simulate tsunamis induced by 2-D submarine landslides.

Summary

Among the lessons learned from the validation of both 1-D and 2-D recreated linear MSE models with a FTCS scheme, three factors demonstrated to play an important role in the behavior of the solution. The first influential parameter is the simulation time over which the solution is computed. Given that the recreated model is being solved in the frequency domain, the solution is assumed to be periodic. In order for the energy to leave the domain and avoid interference, the simulation time should be long enough. Simulation times of 500 s were found to be adequate in this regard and to yield converged solutions. Secondly, the water depth utilized to calculate the filter

function must equal the water depth without the landslide, not to be confused with the water depth symbolizing the slide passage. Lastly, the sequence of operations associated to the MSE source term must be strictly followed. This sequence is commenced by taking the second-time derivative of $h_p(x,t)$ which describes the landslide motion; then, followed by taking the Fourier Transform of the differentiated water depth or forcing function; next, followed by the computation of the filter function using the baseline water depth $h_o(x)$; and finally, terminated by multiplying the transformed forcing function by the filter function. An additional requirement when using the recreated MSE model is multiplying the frequency-domain source term or the time-domain solution by a factor of two.

In order to carry out the probabilistic application narrated in the next chapter, the presented MATLAB-coded numerical experiments were translated to the Fortran 90 language without any shortage of operational capability and compiled using Intel(R) Visual Fortran 11.1.051. For the Fortran 90 version of the 1-D model, the forward and inverse Fourier Transforms subroutines were obtained from Press et al. (1992) and the tri-diagonal matrix solver from Dr. James Kaihatu, Texas A&M University. Subroutines for the Fortran 90 version of the 2-D model were all taken from Press et al. (1992). Comparisons between the solutions provided by both interfaces (i.e., MATLAB and Fortran 90) demonstrated exceptional agreement. To the benefit of this research, the performed computer language translation resulted in a significant reduction of the computational time needed to obtain free surface elevations, especially when running the 2-D models.

CHAPTER V

APPLICATION OF A PROBABILISTIC

MODEL OF MONTE CARLO TYPE

Having shown the satisfactory performance of the MSE model in reproducing the passage of and waves excited by submarine landslides, the probabilistic component of this study will be the focus of this chapter. Watts (2004), Maretzki et al. (2006), and Grilli et al. (2009) demonstrated that Monte Carlo simulations can provide a closed-form solution to a problem susceptible to the behavior of multiple independent variables by supplying initial conditions to a numerical model from a statistical sample. Moreover, Geist and Parsons (2006) point out that a Monte Carlo approach is primarily suitable for analyses of wide geographical regions where multiple sources of uncertainty and scarcity of data exist. Therefore, the adoption of a Monte Carlo method to conduct a probabilistic study of submarine landslide tsunamis is well supported, in view of the complexity of the problem and previous successful applications of this method. In this light, the probabilistic component of this study is founded on Monte Carlo simulations.

Objectives and Limitations of the Probabilistic Study

The purpose of this probabilistic study is to provide a first-order approximation to the hazard posed by submarine rigid landslides in a computationally efficient manner by means of Monte Carlo simulations. In particular, to complement the work that has been carried out in previous risk assessments, the hazard associated to submarine landslides that separate into multiple rigid pieces as failure develops will be the main focus. The strategy is to utilize the outcome of thousands of numerical simulations with the recreated MSE model to complete two tasks. The first task, directed toward advancing the knowledge of submarine-landslide generated tsunamis, is to analyze the influence that the various landslide parameters has on the height of the generated waves.

The second task, oriented toward facilitating the integration of submarine landslide tsunamis into engineering design, is to provide meaningful wave probability distributions that can be easily interpreted. To accomplish the latter, emphasis is given to the waves triggered by submarine landslides that propagate toward the shore.

Despite the use of the same Monte Carlo methodology, this investigation presents several differences from the referenced probabilistic studies. No geographical region is particularly targeted, thus sediment parameters, as will be discussed next, are generalized and seafloor profiles are approximated as flat slopes. Furthermore, landslide motion is assumed to occur at $t = 0$ with an acceleration given by Equation (22), hence discarding seismic forcing and slope stability from the calculations. In spite of this, the slide dynamics follow the same analytical expressions (Watts 1998) as those of the three probabilistic assessments used as reference. Breaking wave heights and run-up measurements are also not contemplated in the calculations; however, maximum run-up could be estimated on the basis of the correspondence principle of Watts (2005), but will not form part of the final outcome. Finally, only 1-D simulations are carried out.

The data collected from the Monte Carlo simulations will be displayed for two cases: a parameter subspace with constant values and a parameter subspace in which one input is singularly varied while the others are held constant. In conjunction with the latter, a sensitivity analysis will be performed on the variable parameter. Although less inclusive than past hazard assessments, the introduction of the multi-piece slide failure mode and the concept of quantifying slide coherency into the present probabilistic model offers a new perspective to the analysis of tsunami characteristics induced by underwater landslides.

Specification of Slide Input Parameters

In addition to the inputs considered in the model validation chapter (i.e., α, Δh, γ, C_d and C_m), three new parameters are needed in the numerical model being fed by the Monte Carlo method. The first new input is the number of pieces (Nc) that will detach

from the submerged mass at rest. This number must be an integer and can be given any value equal to or greater than 1. The second parameter is the baseline water depth (i.e., the water depth without the slide) to thickness ratio (*doI*) passing through the slide center of mass. The third parameter, labeled *delay*, is the dimensionless scaling factor delimiting the time taken for the initially-at-rest, single-piece slide to completely fail (i.e. to detach into *Nc* pieces). The larger the value assigned to *delay*, the longer the failure. In addition, this set-up requires slide width parallel to slope as an input, but in the form of a dimensionless ratio of slide width along slope to slide thickness, denoted by *b'*. Finally, bottom slope is entered in its fractional form (e.g., 1/5) and is represented by β.

In total, not counting the fixed value of Δh, there are eight inputs to the model. Five of these inputs (β, *b'*, *Nc*, *doI*, and *delay*) are to be deterministically specified, meaning the user has the ability to select values for these variables at his/her own discretion. The remaining three inputs (γ, C_d, C_m) are to be probabilistically defined, meaning random distributions must be assigned to them. Given their presence in the slide equations of motion, all eight parameters will influence the evolution of the submarine failure and the subsequent free surface response.

Deterministic Slide Parameters

The deterministic inputs can virtually be given any value; however, parameters *b'* and *doI* are constrained by two conditions. On the one hand, any combination of values of these two inputs should not expose any portion of the slide above the still water level. In other words, the slide must be fully submerged at all times. On the other hand, values for *b'* and *doI* are restricted by the length of the horizontal domain because the slide cannot be placed at an offshore distance that will not allow the collection of wave data from the points of interest on the free surface (these points will be defined later in this chapter). Parameter β also influences the range of values for *b'* and *doI* that can satisfy the conditions just mentioned. The smaller the value of β, the narrower the

acceptable value ranges for *b'* and *doI*. Beware, however, that MSE models may become inaccurate for β greater than 1/3 (Demirbilek & Panchang 1998).

Initially, C_d had been classified as a probabilistic parameter. The normal distribution that was given to it, however, resulted impractical due to the defective behavior of the right boundary condition. In the range where $C_d < 0.8$, the first detached slide piece was observed to move fast enough to exit the domain before the entire failure had reached an end, thus allowing for reflected waves. Therefore, C_d was assigned a constant value of 1.0 as suggested by other studies in the literature that use the presented set of equations to model submarine landslides.

Randomized Slide Parameters

The remaining inputs (γ and C_m) are to be probabilistically inserted into the model. Here, this is done by defining for each of these parameters a probability density function (PDF) formulated using available field and experimental data in the literature. Grilli et al. (2009) take a similar approach in defining random distributions for their Monte Carlo set of inputs which they prescribe by means of normal, log-normal, and uniform distributions. Unfortunately, this study only shares one probabilistic input in common, corresponding to γ, with their stochastic analysis. Hence, the two probabilistic parameters in the present study are assigned normal distributions due to the simplicity of such PDF and the absence of better guidance in the literature.

To construct a normal distribution, a mean (μ) and a measure of the distribution of the population about the mean, known as standard deviation, must be specified. For a given μ, the unbiased standard deviation (σ) is given by

$$\sigma = \sqrt{\sum \frac{(X - \mu)^2}{N-1}} \tag{33}$$

$$\sigma_r(\%) = \left(\frac{\sigma}{\mu}\right) \tag{34}$$

where X is the population set, N the number of elements in the set, and σ_r the relative standard deviation expressed as a percentage. For normal distributions, 68% of the population is within one standard deviation, 95% within two standard deviations, and 99% within three standard deviations from the mean.

The normal distribution of γ was designed to be applicable to the sediment encountered on the ocean bottom at continental margins. According to Almagor (1982), γ of marine sands and silts averages 2.65 while that of marine clayey sediments ranges between 2.40 and 2.85. This is a mere generalization of a much broader spectrum of soil types found on the seafloor. Given the unrestricted application of the model to a particular geographical region, the assortment of soils considered by Almagor (1982) will suffice for the moment. Taking $\mu = 2.65$ and using the γ values of 2.40, 2.65, and 2.80 as X results in $\sigma_r = 12\%$ and a normal distribution for γ as shown in Fig. 5a.

Fig. 5b shows the normal distribution corresponding to C_m. This is the parameter with the greatest uncertainty due to the lack of data related to C_m values suitable for submarine landslides. Nevertheless, the laboratory experiment completed by Watts et al. (2000) in which a fully submerged semielliptical body slides down an incline indicates that $C_m = 1.0$ is a conservative approximation. A value of $C_m = 1.2$ is also found in this experimental work. Therefore, a normal distribution with $\mu = 1.0$ and $\sigma_r = 20\%$ was assigned to parameter C_m. The latter percentage was calculated using values of 1.0 and 1.2 as the population set.
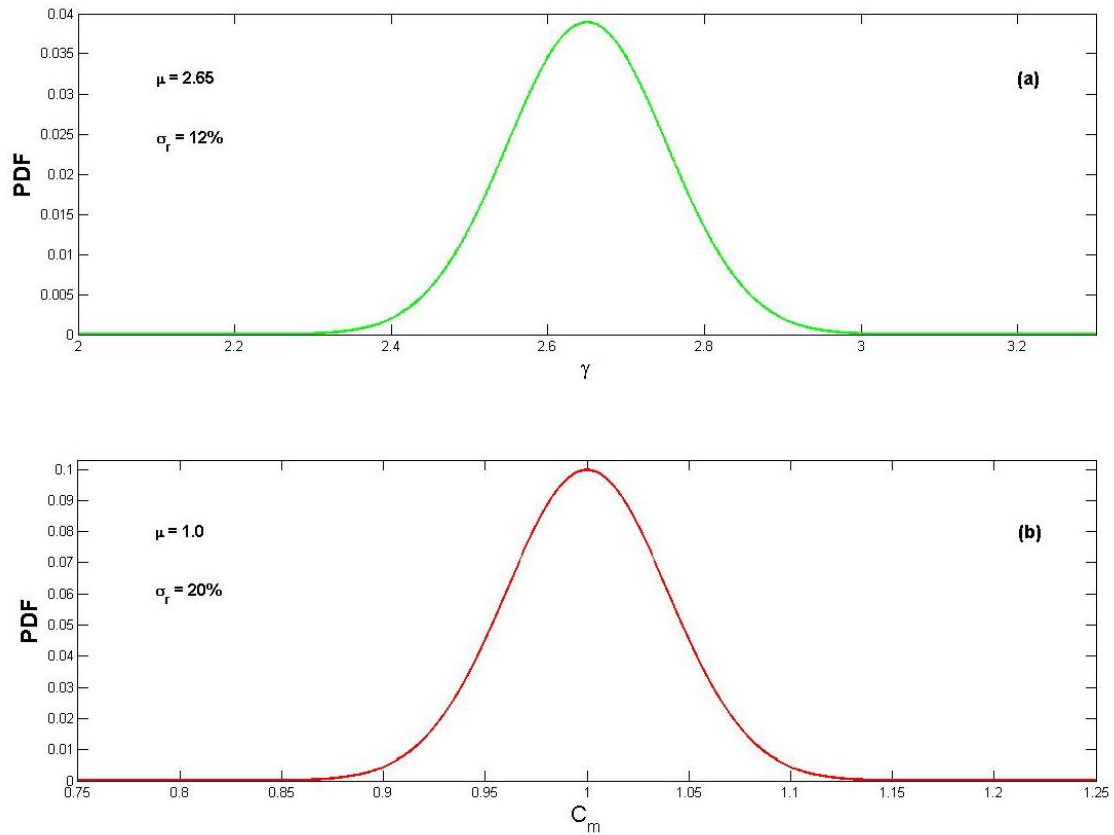
FIG. 5. Normal Distributions of Probabilistic Slide Input Parameters: (a) Specific Gravity (γ) and (b) Added-Mass Coefficient (C_m).

Structure of Adopted Monte Carlo Method

The diagram in Fig. 6 is the step-by-step numerical procedure required to obtain wave height distributions for a parameter space in which one deterministic parameter is allowed to vary while the others remain constant. The same process is followed for a parameter space of constant values if the second, third, and eighth steps in the diagram are removed.
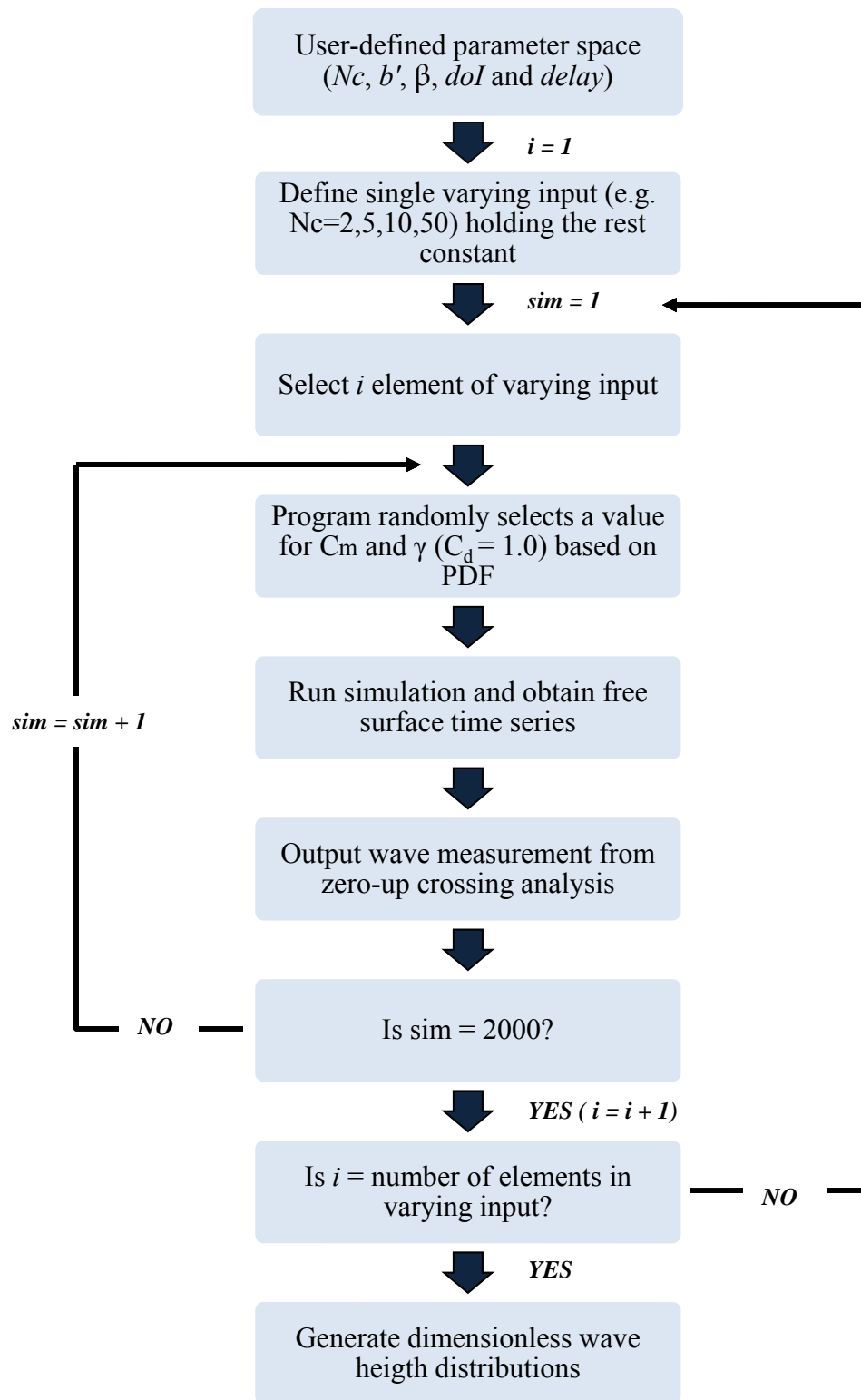
FIG. 6. Monte Carlo Method Diagram Exemplifying the Adopted Numerical Procedure

Numerical Set-Up for Multi-Piece Slide Failure Simulation

The numerical set-up which serves as the core of the designed Monte Carlo simulations will be next described. The slide dynamics of this set-up are the same as those discussed in the model validation chapter and describe a body sliding down a flat slope with an initial acceleration that decays over time until a terminal velocity is attained. Although this scheme is preserved, some additions were implemented into the equations composing the Monte Carlo numerical set-up in order to grant slides the capability to separate into multiple rigid pieces when failure is initiated. In light of this feature, these slides will be referred to as detachable or separable slides in the next paragraphs. As before, the objective is to obtain a water depth function capable of describing the movement of multiple, potentially infinite, slide pieces which dislocate from a single mass. Once the forcing function (i.e., the water depth) is computed, the remaining process of solving the elliptic MSE and recovering the time-domain solution is kept unchanged.

Recalling the methodology followed in the model validation section, an expression for center of mass motion had to be derived in order to model the passage of the slide. Likewise, such an expression will be developed for the mass centers of the multiple pieces that may detach from the single-piece slide at rest. Even though this parent slide is allowed to separate, it is inherent in the equations that follow that the detached slide pieces cannot further separate into smaller fragments and do not undergo deformation of any type. Watts and Grilli (2003) showed, in fact, that slide deformation has little impact in tsunami generation. Moreover, the following set of equations is to be used with $\Delta h = 1$ m. The linearity of the model permits the solution obtained under this assumption to be scaled to thinner or thicker landslides by simply multiplying the time-domain solution times the desired thickness. Note that, as shown in Fig. 2, thickness is defined as the maximum vertical height of the slide.

With this in mind, the process aimed at formulating an expression for the center of mass of a separable slide begins with the specification of the nondimensional

deterministic parameters. Once these are defined, the model selects values for the probabilistic inputs, allowing for initial acceleration (a_o), terminal velocity (u_t), and characteristic time of motion (t_o) to be computed using Equations (22), (23) and (26), respectively.

Equations Governing Slide at Rest

In order to facilitate the mathematical description of the motion, the dynamics of the slide and the pieces it may separate into will be formulated in the horizontal plane and in the end projected onto the sloped plane. Hence, the horizontal width of the parent slide (b_{ho}) and its initial midpoint offshore position (xoI_o) are

$$b_{ho} = b' * cos(\alpha) * \Delta h \qquad (35)$$

$$xoI_o = \frac{doI * \Delta h}{\tan(\alpha)} \qquad (36)$$

The quantities defined by Equations (35) and (36) are necessary to determine the spatial location of the various slide pieces before failure occurs. To accomplish this, the width of the slide pieces must be specified so that the individual slide midpoints can be located. A random number generator (*rand* in MATLAB, *random_seed* in FORTRAN 90) is used to select an Nc number of values ranging from 0 to 1. Each of these numbers is normalized by the sum of all Nc randomly generated values, creating a set of non-dimensional widths (S_w). Multiplying this set by b_{ho}, however, yields the dimensional horizontal width (b_h) of the slide fragments. The midpoint of each slide chunk can now be determined by means of geometrical relationships. Fig. 7 is a preview of the submarine mass failure considered in this probabilistic analysis showing, for $Nc = 3$ and $t = 0$, the static features of the slide pieces, projected on the horizontal plane, that compose the coherent mass resting on the incline. Even though more steps have to be covered to delineate the shape of the displayed slides, this figure provides a helpful

depiction of the variables that have been introduced and the ones that will be next addressed which describe the motionless state of the slides.

FIG. 7. Set-Up of 1-D Submarine Slide ($Nc = 3$) Showing the Horizontal Projection of the Rigid Pieces in Which the Slope-Resting Slide Will Detach ($ts_1 > ts_2 > ts_3$).

Considering that the midpoint of the single-piece slide is known (given by xoI_o), the horizontal midpoint location of slide 1 (xoI_1 in Fig. 7) can be calculated by noting that this body has to share the same x_l location as that of the parent slide. Consequently, the midpoint of slide 1 can be found by adding half of its horizontal width to the point $x = x_l$. In mathematical terms

$$xoI_1 = xoI_o - \left(\frac{b_{ho}}{2}\right) + \left(\frac{b_{h1}}{2}\right) = x_l + \left(\frac{b_{h1}}{2}\right) \tag{37}$$

where b_{h1} is the horizontal width of slide 1. In fact, Equation (37) applies to all leftmost slides as long as the reference midpoint point is that of the single-piece slide. The midpoints of slides 2 and 3 are found by following the same reasoning, but ensuring that the correct reference midpoint is selected. Thus, the general structure of Equation (37) suitable for the slide chunks resting down slope of the leftmost slide piece is

$$xol_i = xol_{i-1} - \left[\frac{b_{h(i-1)}}{2}\right] + \left[\frac{b_{h(i)}}{2}\right] \tag{38}$$

where the subscript i is an integer ranging from 2 to Nc for $Nc > 1$.

The next phase of the computational procedure oversees the start motion times of the slide fragments. Relying on the same random number generators mentioned above, the times at which the slide pieces fail can be imposed. First, a random set of numbers (ts') of size Nc is created in the following manner

$$ts'_i = ts'_{(i-1)} + r \tag{39}$$

where r is a randomly generated number in the [0,1] range and subscript i conserves its previous definition. The value of ts'_1 is arbitrarily set to zero. Actual onset motion times (ts) are produced by carrying out the operation below

$$ts = \frac{ts'*t_o*delay}{ts'_{Nc}} \tag{40}$$

in which normalization by the greatest ts'-value corresponding to $i = Nc$ has been performed. Equation (40) creates a row vector whose values increase with i, suggesting an order of motion for the slide pieces contrary to that shown in Fig. 7 where the leftmost slide piece (slide 1) mobilizes last. The correct hierarchy of motion, as indicated above each slide chunk in Fig. 7, is obtained by flipping row vector ts about a fictitious horizontal axis to arrange the values of ts in decreasing order from left to right with the

greatest value occupying the first entry and zero, or any other arbitrary motion initiation time, taking the last entry. The next group of formulas assumes row vector *ts* has been flipped.

Space-Time Slide Coherency

A quick review of the equations that have been formulated thus far indicates that Equations (35) to (40) permit, at a motionless state, the calculation of the width, midpoint location, and triggering time of multiple slides which disjoin from a single mass of known width and midpoint position. Although start motion times act as an indicator of how many seconds apart from each other the slides pieces disjoin, they do not provide insight on how compact or spread the overall failure is when the width of each fragment is factored in. The randomness involved in the determination of triggering times as well as in the estimation of the width of the detached pieces demands a better representation of the coherency of the parent slide doomed to fail. In other words, an indicator of whether the single-piece slide will behave as *Nc* entities moving in close proximity to each other or as *Nc* pieces individually failing with little or no interaction between them is sought. Not only would such indicator provide insight on the failure progression of the submarine mass, but it would also aid in conceiving the extent at which the detached slide pieces combine their effects in the evolution of the free surface. In this study, the concept of slide space-time coherency (Ω) is contemplated through an ad-hoc formula of the following composition

$$t_{\Omega(j,k)} = {}_{j=1}^{Nc} \left\{ {}_{k=1}^{Nc} \ abs\left(ts_j - ts_k\right) * delay \right\} \tag{41}$$

$$\Omega_{(j,k)} = {}_{j=1}^{Nc} \left\{ {}_{k=1}^{Nc} \ \Omega_{(j,k-1)} + \frac{sw_k}{[(1+t_{\Omega(j,k)})]} \right\}; \ \Omega_{(j,0)} = 0 \tag{42}$$

where t_Ω is the time difference in onset motion times between a single slide fragment and the rest of the slide pieces scaled by the specified *delay* value, and subscripts *j* and *k* are integers ranging from 1 to *Nc*. The variables t_Ω and S_w conceptually represent, respectively, the temporal and spatial components of Ω. Thus, Equation (42) is an estimation of the correlation between size and start motion time of each slide piece with respect to the other pieces. Numerically, using FORTRAN 90 syntax, Equations (41) and (42) can be combined into a nested loop as shown in Appendix A.

The final space-time coherency of a particular single-piece slide varies from 0 to 1 and is given by the greatest value contained in the Ω array. As this variable approaches its lower bound, the slide is more likely to behave as *Nc* independent pieces of similar size. The minimum possible Ω value depends on the value assigned to *Nc* and is defined by 1/ *Nc*. In this case, the parent slide is expected to fail in the form of *Nc* fragments of equal width moving independent of each other. On the contrary, when Ω nears its upper bound, the overall failure behavior approximates that of a single coherent mass, implying that the slide chunks move close to each other. Regardless of the size of the parent slide, $\Omega = 1$ whenever $Nc = 1$.

Applying the introduced space-time coherency concept to the example portrayed in Fig. 7, Equation (42) yields $\Omega = 0.4613$ for a slide having the following inputs: $Nc = 3$, $b' = 50$, $doI = 6$, $\beta = 1/10$, and *delay* = 10. Given the minimum Ω is around 0.3 for this scenario, the computed Ω suggests that the slide chunks will have moderately different widths and will be mobilized distinctively apart from each other, therefore insignificantly combining their effects in the initial failure stage. This is verified by examining the dimensional widths and onset motion times for $\Omega = 0.4613$, corresponding to case (2) in Table 1. The rest of the cases shown in this table exemplify the purpose of the Ω function in describing the spatial and temporal characteristics of the slide failure.

Table 1. Space-Time Coherency Values for the Slide Shown in Fig. 7

	b_{h1}	b_{h2}	b_{h3}	ts_1	ts_2	ts_3	Ω
Case (1)	15.8	16.3	17.7	36.04	18.3	0	0.3580
Case (2)	10.3	22.8	16.6	36.04	24.3	0	0.4613
Case (3)	32.4	11.2	6.1	36.04	5.58	0	0.6531
Case (4)	41.4	4.3	4.1	36.04	1.88	0	0.8322
Case (5)	2.9	46.7	0.12	36.04	14.4	0	0.9392

The Ω values presented in Table 1 demonstrate that as Ω approaches 1, the slide pieces have to either move in closer proximity to each other (Case 3) or acquire disproportional sizes (Case 5). Conversely, the smallest value of Ω indicates a more spread slide failure where the slide chunks become more independent of each other and attain similar widths (Case 1).

Before transitioning to the portion of the model that oversees slide dynamics, the mass of the single-piece slide and the combined mass of the slide chunks need to be calculated. These masses are not equal due to the randomness associated to the prescription of the widths of the slide fragments. In theory, however, the detached slide pieces should possess the same mass as that of the parent slide. Hence, the difference in masses between the original slide and its fragmented pieces in the form of a ratio is sought in order to properly scale the water depth function that will define the overall failure. To compute the mass of any of the four slides shown in Fig. 7, for example, the function that outlines their shape or the water depth profile must be specified. Removing the h_o term from Equation (28), the water depth profile (*ellip*) is

$$ellip\,(x) = \tfrac{1}{4}\Delta h\left\{1 + tanh\left[\tfrac{x-x_l}{s'_f}\right]\right\}\left\{1 - tanh\left[\tfrac{x-x_r}{s'_f}\right]\right\} \tag{43}$$

where x_l and x_r retain the same geometric and mathematical definitions given by Eqs. (29) and (30) with the exception of the variable x_c which must be replaced by *xoI*. Notice that *xoI* is not a function of time because it is calculated at rest; thus, x_l and x_r have a single value here. The steepness factor (S'_f) in Equation (43) also maintains its original definition (Equation 31) with the prime indicating the substitution of 0.5 in the numerator by $\pi * \Delta h$. If the value of *xoI* is that of the single-piece slide, then the addition of the evaluation of Equation (43) at each node in x yields the mass (m_s) of such slide, namely

$$ m_{s(ii)} = m_{s(ii-1)} + ellip_{ii} \quad ; \quad m_{s(0)} = 0 \tag{44} $$

where subscript *ii* is an integer ranging from 1 to the number of step sizes (*nx*) in the discretized x-domain. Equation (44) is also applicable to the masses of the slide pieces disjoining from the parent slide. The overall mass of these pieces (m_m) is equal to the sum of their individual masses. A mass ratio of parent slide mass (m_s) to the combined mass of the disjoined slides (m_m) can now be computed, here denoted as m_R.

Formulation of Multi-Piece Slide Motion

In order to model the down slope displacement of the slides in Fig. 7, the time dependency of the multiple centers of mass must be incorporated into Equation (43). This was achieved in the model validation chapter through Equation (32). Comparing the elements of the latter equation with what has been computed so far in this chapter, it is evident that an equivalent expression for s (center of mass motion) valid in the context of multiple slides progressively failing is missing. Such expression must contain information regarding the displacement of each slide fragment as a function of start motion time and terminal velocity development.

Prior to motion, a slide piece remains stationary with zero velocity. Once triggered, the velocity of the slide piece begins to evolve with time according to an alternate form of Equation (28) which better suits multi-slide submarine failures, namely

$$u_c(t) = u_t * tanh\left(\frac{t_n - ts_j}{t_o}\right) \tag{45}$$

where u_c is the time-dependent velocity of a slide chunk, subscript n is an integer ranging from 1 to nt, and subscript j is an integer going from 1 to Nc. For times $t < ts$, u_c = 0. However, when $t \geq ts$, Equation (45) indicates that, once set in motion, the velocity of a slide piece will rapidly increase mimicking the behavior of the hyperbolic tangent, attaining its maximum value (i.e., u_t) when the trigonometric function reaches its asymptote. Therefore, despite of their difference in size and onset motion time, all the slide chunks acquire the same terminal velocity.

The displacement that the slide pieces undergo as their velocity evolves also needs to be calculated. On the horizontal plane, the traveled distance (ds) experienced by each slide piece is given by

$$ds_n = ds_{(n-1)} + u_c * dt \quad ; \quad ds_0 = 0 \tag{46}$$

which becomes effective for times $t \geq ts$. The horizontal center of mass motion for each slide fragment can finally be prescribed as follows

$$x'_c(t) = xoI + ds * cos(\alpha) \tag{47}$$

where the prime in x'_c has been inserted to distinguish this variable from the one used in Equation (32). The right and left inflection points of each slide piece as it travels, x_l and x_r, respectively, are found through Equations (29) and (30) with the center of mass motion given by Equation (47). With this, the passage of the slide pieces on the

horizontal plane can be entirely modeled from triggering to zero acceleration. The projection of the failure onto the sloped plane is obtained in the following manner

$$h'_p(x)_j = h'_p(x)_{j-1} - \mathfrak{m}_R * ellip(x)_j \quad ; \quad h'_p(x)_0 = h_o(x) \tag{48}$$

where h'_p is the function describing the water depth profile of all slide pieces over the x-domain and subscript j is an integer ranging from 1 to Nc. The prime in h'_p is used to distinguish the applicability of Equation (48) to multi-piece slide failures from Equation (28). Note the implementation of the previously calculated mass ratio which adjusts the mass of a slide piece to the overall slide mass distributed among the various detached pieces. Also notice from the subscript arrangement in Equation (48) that the slide chunks are modeled one over the other from leftmost to rightmost except for the leftmost piece which is modeled over the original baseline water depth (h_o). It is this arrangement that allows the creation of a single, undivided slide before failure occurs rather than Nc slide fragments overlapping each other like the three slides projected on the horizontal plane in Fig. 7.

The process enclosed by Equations (45) to (48) is repeated for all slide pieces at each time step to model the translation of each piece and obtain the combined passage of the Nc slide chunks. Therefore, the failure evolution of a single-piece slide that separates into various pieces is

$$h_{Nc}(x,t) = h'_p(x)_{Nc} \tag{49}$$

where h_{Nc} is the combined water depth of all disjoined slide pieces or when $j = Nc$ in Equation (48). Equation (49) represents the water depth that will become the forcing function of the linear MSE model so that the response of the free surface to the bottom motions can be assessed. To more clearly illustrate the procedure outlined by Equations (43) to (49), the Fortran 90 code lines that address this section of the solution computation are presented in Appendix B. Using the same parameters with which the Ω

values in Table 1 were calculated and $C_d = C_m = 1.0$, $\gamma = 2.65$, a snapshot of the slide shown in Fig. 7 undergoing failure is presented in Fig. 8. For ease of visualization, η has been multiplied by a factor of 10 in this figure.
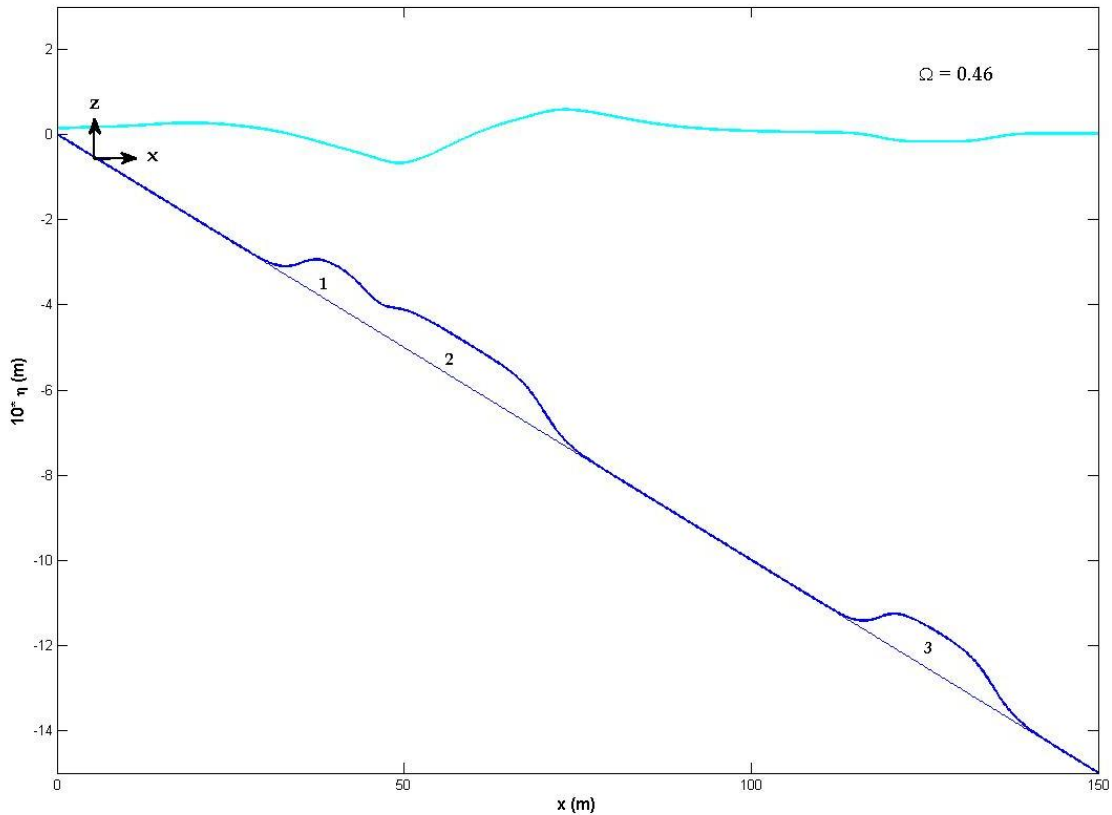
FIG. 8. Free-Surface Response and Ground Motion Corresponding to the Failure of the Single-Piece Slide Shown in Fig. 7 ($Nc = 3$).

Collection of Wave Measurements

To finalize the numerical procedure and obtain information about the triggered waves, the model records the time series of the free surface at different points within the domain. These locations correspond to $x = xoI_o - (b_{ho}/2)$, $x = xoI_o$, $x = xoI_o + (b_{ho}/2)$, and $x = xoI_o + (3\ b_{ho}/2)$. Through these points of interest, a sense of what is occurring to the

free surface above the rear, middle and front of the slide as well as farther offshore can be conceived. A zero-up crossing analysis on each time series is then implemented to obtain the magnitude and number of crests, troughs, heights, and periods of the generated waves. These time series, however, do not account for the entire simulation time, but only up to when the first disjoined slide piece reaches the right boundary to avoid the false reflected waves. In addition to this modification, an extension was added to the standard zero-up crossing analysis to account for any crests or troughs anteceding the first zero-up crossing. Though this "first" elevation or depression is not a complete wave, it is assigned a period equal to the length of the time series minus the sum of all the recorded wave periods.

Fig. 9 shows the time series recorded at the four prescribed locations for a slide with the same parameters as in Fig. 8 except *delay* = 30 (Ω = 0.4586). Subplot (a), representing the landward limit, shows that each slide piece generates a surface depression that travels shoreward. As expected, the second depression is the largest one because it corresponds to the biggest slide piece. Fig. 9b also displays three distinct disturbances, being the one associated to the last piece to move the most prominent one. This is due to the fact that when a slide piece fails, it gives subsequent pieces more room for their triggered waves to evolve before these waves are captured by the time series-recording point above the slide middle. Showing a better picture of the offshore wave field, Fig. 9c portrays the crests of the triggered waves and the trough that travels with the slide front. The amplitude of both crests and troughs is in agreement with the size of the slide fragments. Moreover, the information provided by Figs. 9a and 9c is congruent with the observations of Jiang and LeBlond (1992) who describe a shoreward traveling trough, an offshore propagating crest, and a forced trough moving with the speed of the slide front. Finally, Fig. 9d shows the evolution of the generated waves as the slides enter deeper water. It is noticeable here that the crests propagate faster than the slide front.
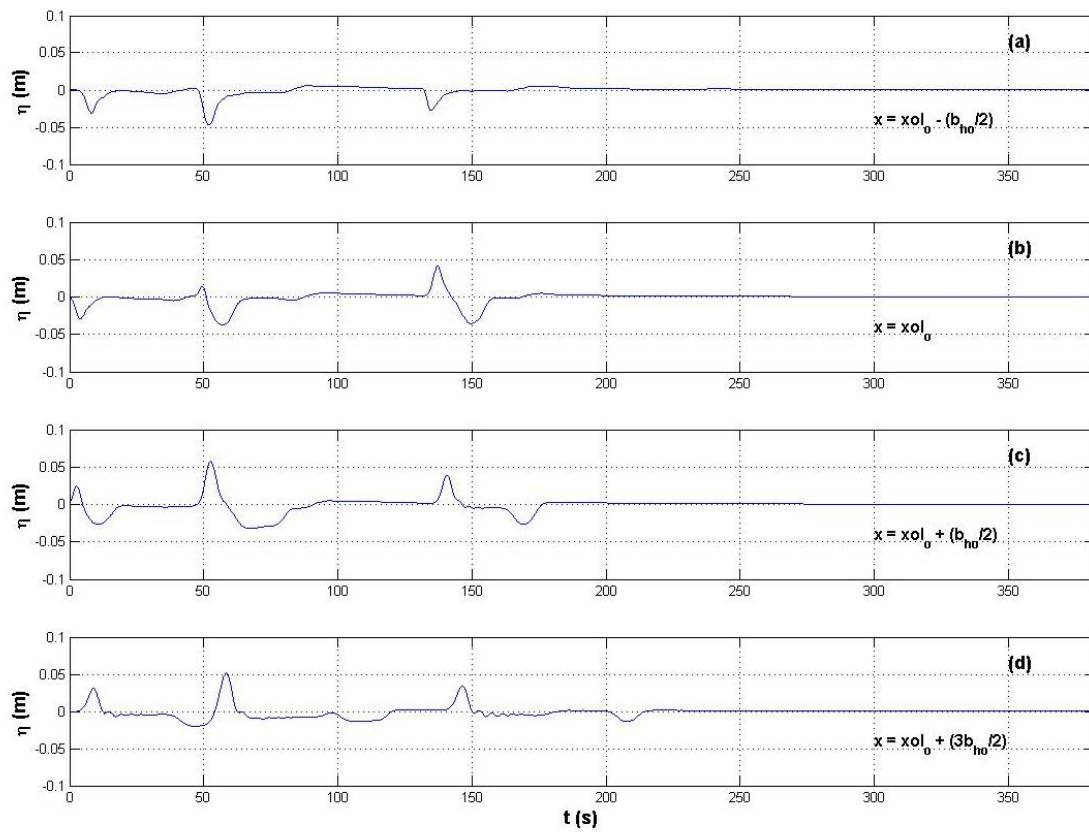
FIG. 9. Free Surface Time Series Captured above the (a) Rear, (b) Middle, (c) and Front of the Single-Piece Slide Shown in Fig. 7. Subplot (d) Corresponds to the Offshore Location.

CHAPTER VI

RESULTS

As indicated in Fig. 6, a parameter space must be specified to commence the Monte Carlo simulations. Table 2 shows the deterministically-selected parameter space with which the results discussed in this section were obtained. These values were chosen with the intention to explore a wide variety of combinations and to facilitate the recognition of the degree of influence of the different inputs on the free surface response. Given the emphasis of this probabilistic study on the waves traveling toward the coast, the parameter space in Table 2 was designed to ensure that gathering of wave data from the landward time series location where $x = xoI_o - (b_{ho}/2)$ was possible while guaranteeing the full submergence of the landslide. This time series location is right above the rear of the landslide at rest (x_l in Fig. 5).

Table 2. Parameter Space for Monte Carlo Simulations

Nc	2	5	10	50	
β	1/10	1/15	1/20	1/30	
b'	10	25	40	75	
doI	5	8	10		
delay	2	5	10	30	60

In total, 960 combinations can be arranged with the parameter space defined in Table 2. Each of one of these combinations undergoes 2,000 runs with varying values of γ and C_m as dictated by their normal distributions. These simulations assume $\Delta h = 1$ m and have a domain size of 800 m, a simulation time of 2047.75 s, a grid consisting of $\Delta x = 0.4$ m and $\Delta t = 0.25$ s, and two lateral open boundaries (the left boundary is flattened at $\eta = -0.25$ m from $x = 0$ to $x = 4.5$ m). The coarseness of the grid is a consequence of the domain size needed to avoid the false reflected waves previously mentioned. Nevertheless, good accuracy is still retained.

Parameter Subspace with Constant Values

To begin the examination of the results, a case where the deterministic parameters have a single value will be first considered. Figs. 10 and 11 show the outcome of this numerical experiment which was conducted with the following parameter subspace

$$Nc = 5 \qquad \beta = 1/15 \qquad b' = 40 \qquad doI = 8 \qquad delay = 30$$
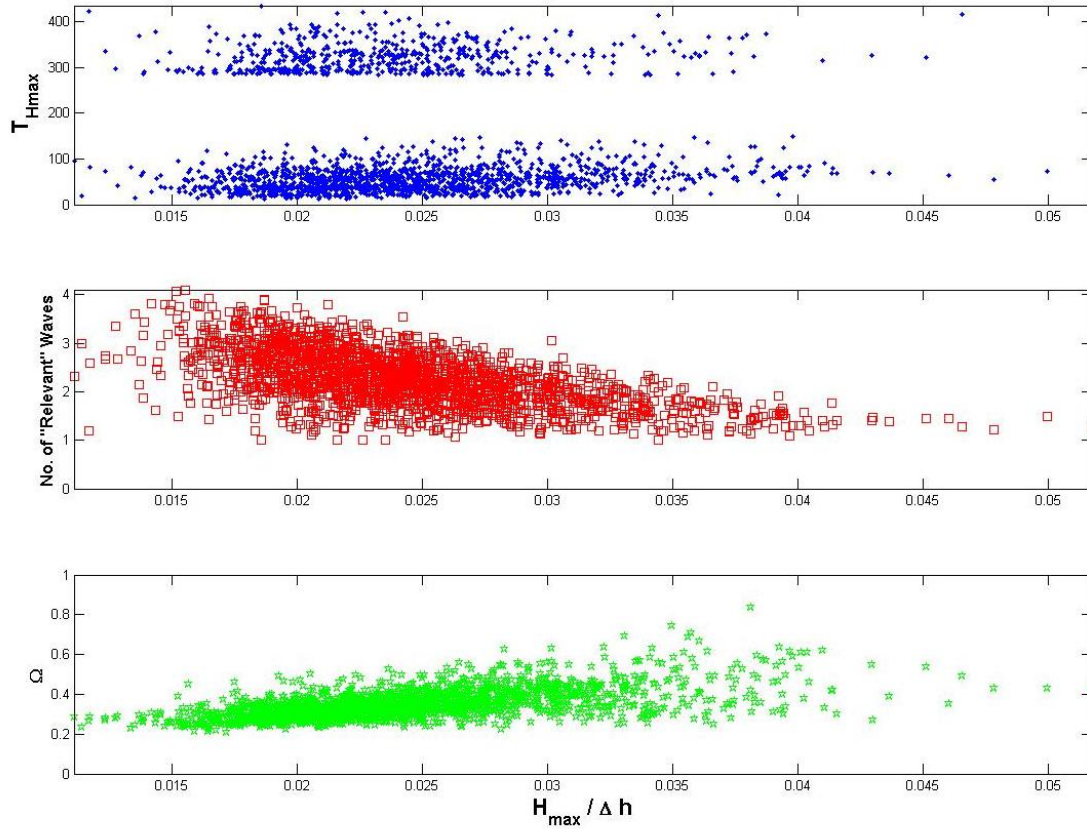
FIG. 10. Nondimensional Maximum Wave Height ($H_{max}/\Delta h$) Charts for a Parameter Space with Constant Values Showing: (a) Period of Maximum Wave Height (T_{Hmax}), (b) Number of "Relevant" Waves, and (c) Slide Coherency (Ω).
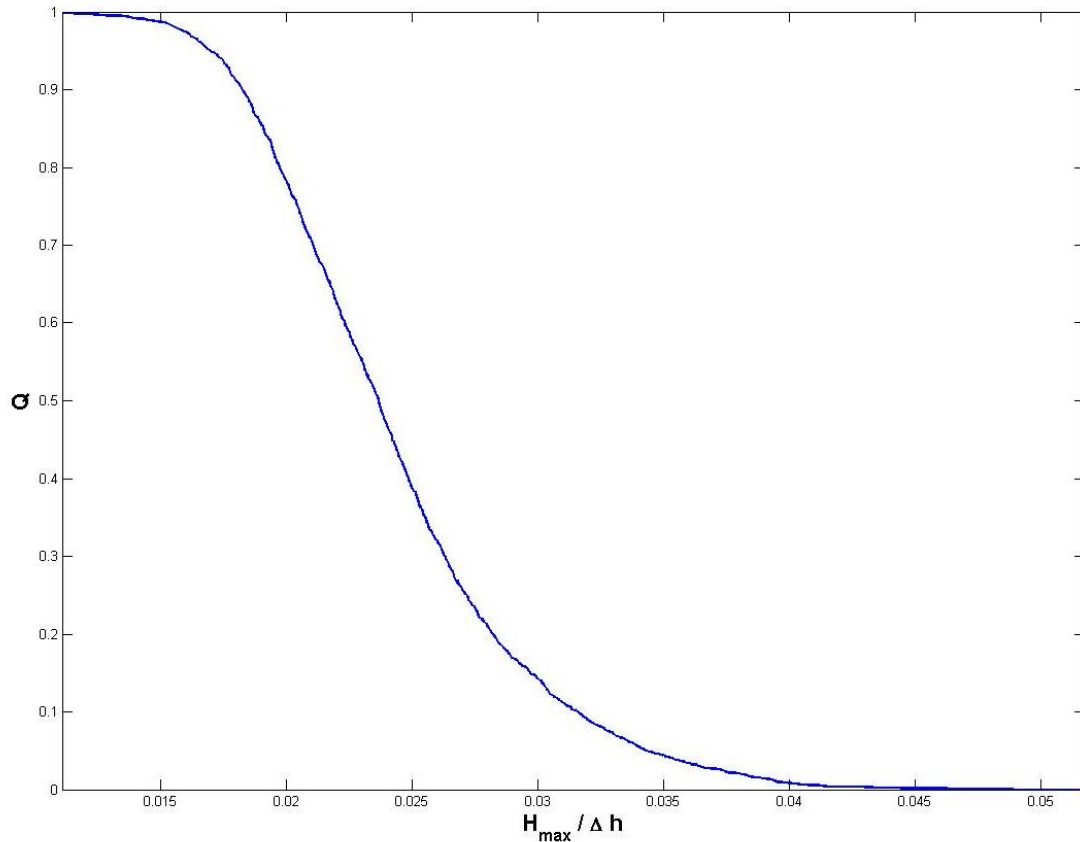
FIG. 11. Probability of Exceedance (*Q*) Curve for Nondimensional Wave Height (*H$_{max}$/Δh*) for a Parameter Space with Constant Values.

Fig. 10a is a scatter chart of the dimensionless periods of the highest waves (*T$_{Hmax}$*) versus maximum nondimensional wave heights (*H$_{max}$/Δh*). Wave periods have been nondimensionalized by an arbitrary characteristic time scale for long wave motion equal to (*g/doI)*$^{1/2}$. This characteristic time scale provides information about dispersion by indicating how many water depths are contained in a wave length. Two groups of results are immediately appreciable in Fig. 10a. The wave periods close to 280 s and above correspond to the periods of the "wave" anteceding the first zero-up crossing (Fig. 9). The second group of periods, ranging from 20 to 140 s, corresponds to the highest waves of the remaining wave record. The ample range in *T$_{Hmax}$* in both groups is descriptive of the frequency dispersion manifestations that are present in the generation

region, thus rectifying the importance of using dispersive models to recreate submarine landslide tsunamis.

To quantify hazard in terms of the number of waves of considerable height that may reach the shore, a wave-weighting operation is implemented into the processing of wave height data to reduce the effect of small wiggles. This operation consists of normalizing the record of wave heights by the maximum height in that record. These weighted waves are then summed to generate a number of "relevant" waves. Fig. 10b shows the result of performing such weighting operation. A trend of decreasing number of "relevant" waves with increasing $H_{max}/\Delta h$ is clearly noticeable. This behavior is, in fact, congruent with the essence of the weighting operation. For this particular parameter subspace, Fig. 10b indicates that up to 4 waves of comparable height to a $H_{max}/\Delta h = 0.015$ may reach the shore. For other parameter subspaces, a maximum of 6 "relevant" waves was discerned.

Furthermore, Fig. 10b provides insight on the characteristics of the slide failure. For a given simulation, the larger the number of "relevant" waves, the more comparable the generated waves are to the maximum wave height. This can only occur if the slide breaks into pieces of similar size. On the contrary, low numbers of "relevant" waves suggest that there is a substantial difference in at least one of the widths of the detached pieces.

Fig. 10c presents the correlation between Ω and the height of the triggered waves. This subplot supports what has been deduced from Fig. 8b in the sense that it shows that slide failures whose coherency is close to that of a single-piece slide (i.e., Ω values approaching 1) tend to create the highest waves and, therefore, the lowest number of "relevant" waves. Despite the evident trend in Fig. 8c, the maximum wave heights do not correspond to the largest Ω values. The reason behind this discrepancy is that low C_m and high γ favored the magnitude of the generated waves of these moderately coherent data points. In spite of this, Ω is observed to be a good predictor of the free surface response to the spatial and temporal features of the slide failure progression. Though an upper bound for Ω cannot be inferred from this subplot, there is a minimum Ω value,

close to 0.21, for the considered Nc. This minimum is acquired when the slide pieces are very close to sharing equal widths.

Lastly, Fig. 11 shows a probability of exceedance (Q) curve for $H_{max}/\Delta h$. This curve provides the direct means to assess, in the probabilistic sense, the tsunamigenic potential of the examined combination of parameters. Wave statistics such as the wave height with 5% probability of being exceeded ($H_{0.05}$) can be extracted from distributions of this kind. For the case being analyzed, $H_{0.05} = 0.0344$. Note this and any statistic of interest extracted from Fig. 11 is dimensionless and must be multiplied by Δh to obtain the actual wave height.

Sensitivity Analysis

The purpose of the sensitivity analysis is to observe how the height of the waves fluctuates in response to the variation of a particular slide parameter. Likewise, this analysis can be used to identify which combinations are the most tsunamigenic and to conceive the hazard associated to these combinations. A parameter subspace will be created from Table 2 and utilized throughout this analysis. Each deterministic parameter will then be singularly varied while holding the rest constant. In the end, tabulated wave statistics for $H_{0.05}$ will be compared.

Bottom Slope and Randomized Parameters

It results convenient to analyze the influence of the randomized inputs (γ and C_m) in conjunction with β because all four parameters are interrelated through the computation of a_o and u_t (Eqs. 22 and 23). Therefore, β will be varied according to the values shown in Table 2 while assigning a single value to the remaining parameters. Figs. 12 -14 show the results associated to the parameter subspace shown below.

$$Nc = 5 \qquad b' = 40 \qquad doI = 8 \qquad delay = 30$$
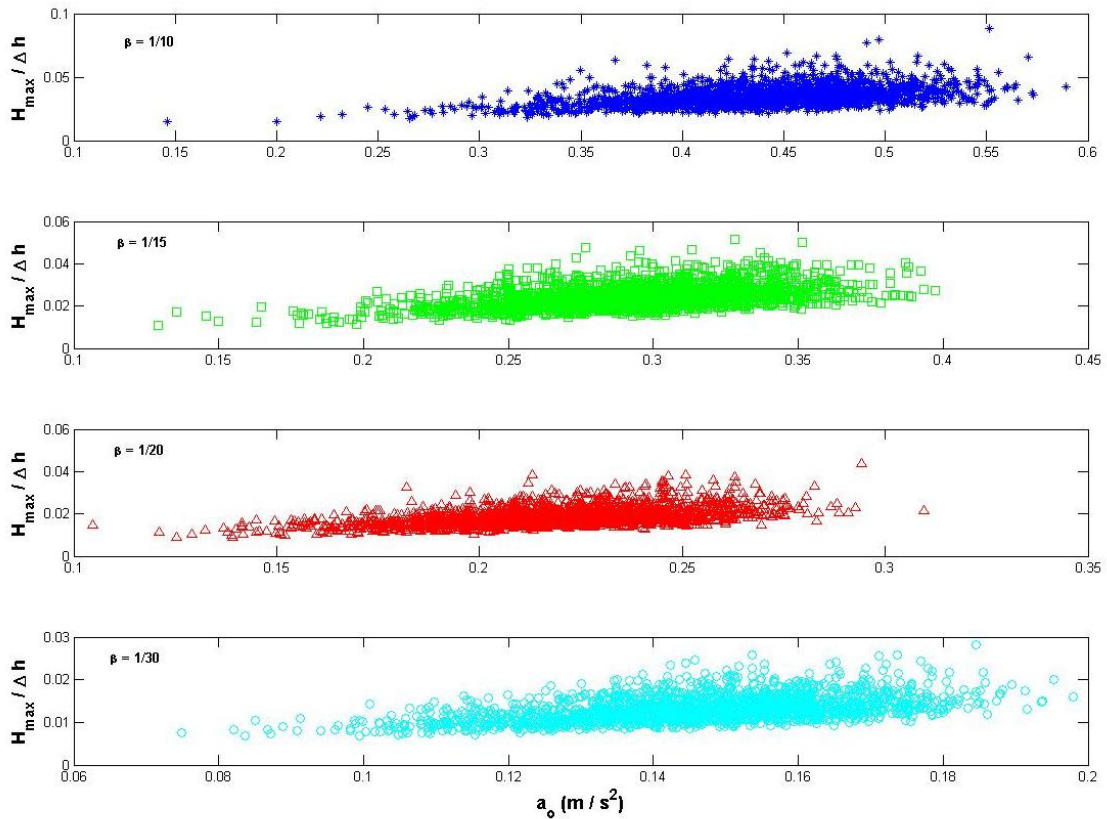
FIG. 12. Relation between Slide Initial Acceleration (a_o) and Nondimensional Maximum Wave Height ($H_{max}/\Delta h$) for Various Slopes: (a) β=1/10, (b) β=1/15, (c) β=1/20 and (d) β=1/30.

Fig. 12 shows how different values of β influence the magnitude of a_o and how the latter relates to the height of the generated waves. It is evident in these scatter charts that values of a_o increase as β becomes steep. Likewise, the increase in values of a_o results in increasing values of $H_{max}/\Delta h$ in a linear-resembling fashion of rather weak character. Although this direct proportionality is clear, the scatter of data in Fig. 12 is owed to the randomization of γ and C_m. Thus, it is worthwhile examining which of the three parameters (β, γ and C_m) involved in the computation of a_o is more dominant. This is the purpose of Fig. 13.
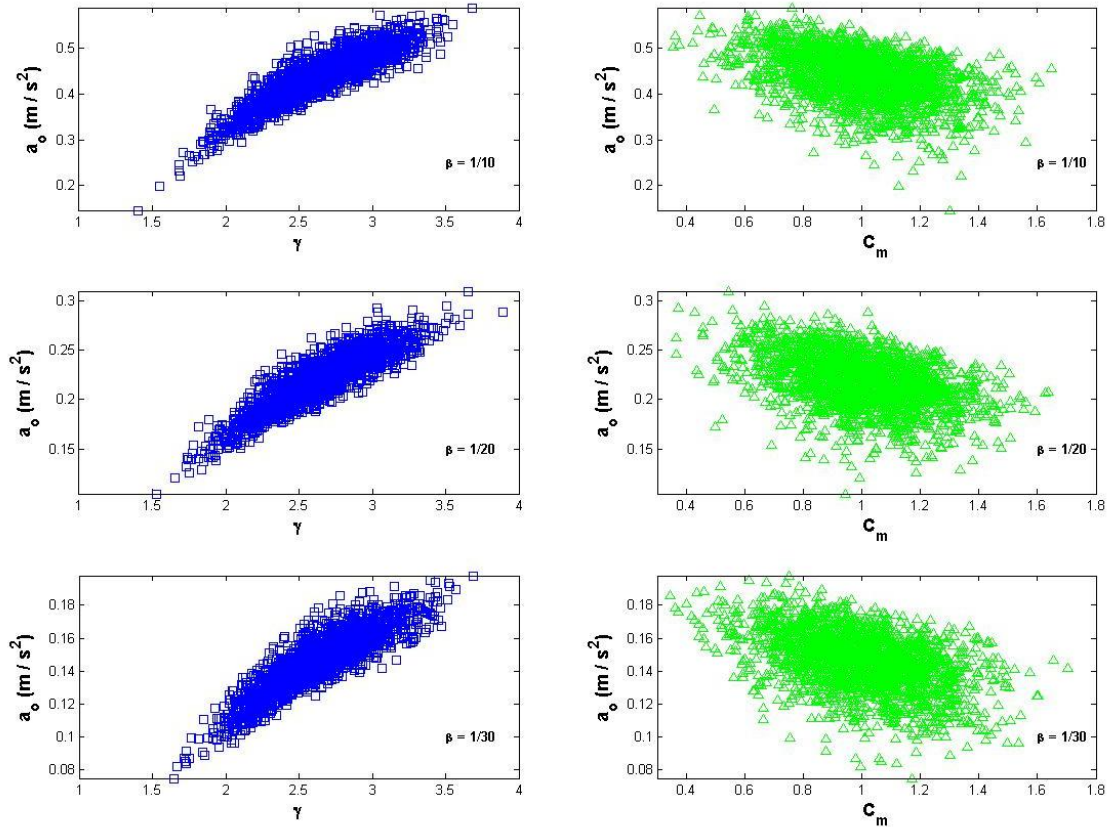
FIG. 13. Slide Initial Acceleration (a_o) as a Function of Specific Gravity (γ) (left panel) and Added-Mass Coefficient (C_m) (right panel) for Various Slopes (β).

Fig. 13 shows the relationship between γ, C_m, and a_o for only three values of β for ease of visualization. Variations in a_o due to the randomized parameters suggest that, for any fixed β, increasing values of γ and decreasing values of C_m correlate to increments in a_o. Thus, it is possible to attribute the trend of increasing values of $H_{max}/\Delta h$ in each individual subplot of Fig. 12 to the increasing and decreasing tendency of γ and C_m, respectively. However, it is also clear from Fig. 13 that, although γ and C_m create appreciable variations in a_o, the magnitude of β is what drives the major increments or decrements of this quantity. In other words, the contribution to a_o of parameters γ and C_m is dominated by the magnitude of β. A similar analysis is not shown for u_t given the

fixed value of C_d and the observed influence of γ on a_o. In spite of this, the same conclusions would most likely be drawn.
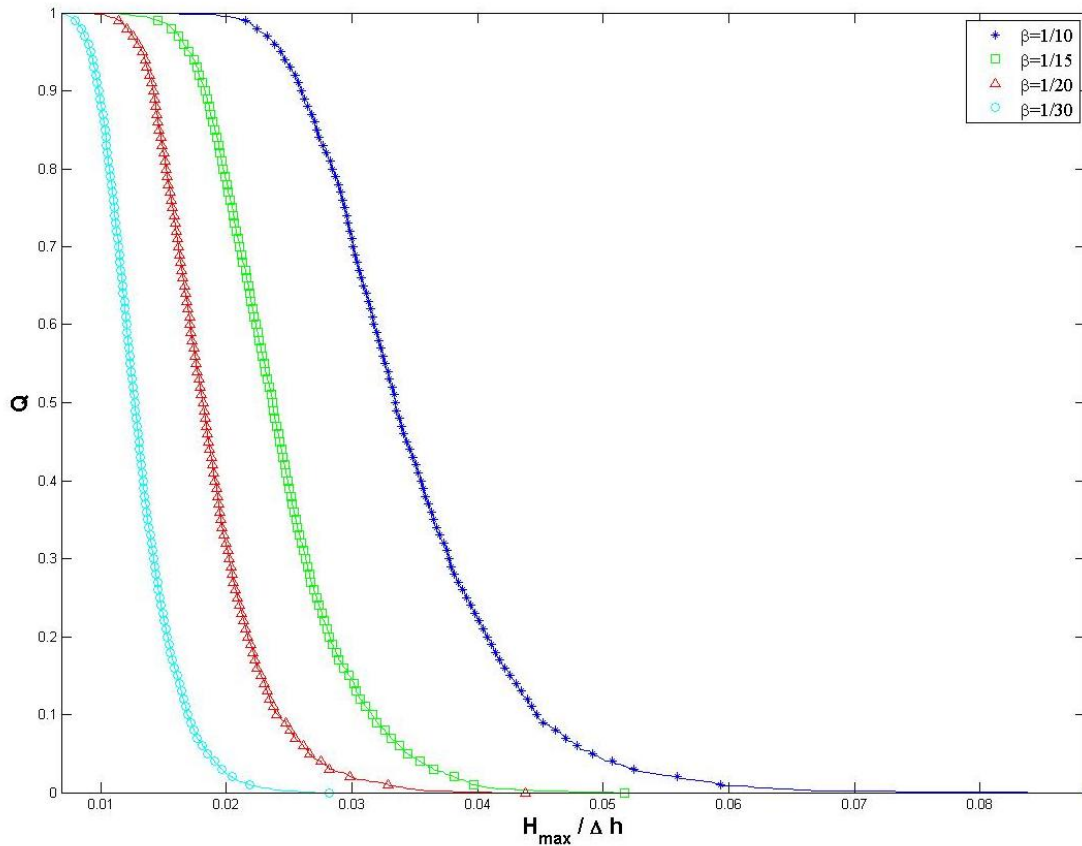
FIG. 14. Probability of Exceedance (Q) Curve for Nondimensional Wave Height ($H_{max}/\Delta h$) for a Parameter Space with Variable Slope (β).

Although Fig. 12 provides insight on the relation between β and $H_{max}/\Delta h$, it is important to directly examine the degree of dependency between these two. To accomplish this, a probability of exceedance curve for $H_{max}/\Delta h$ for each β value was constructed and is presented in Fig. 14. In this figure, values of $H_{max}/\Delta h$ are observed to diminish as β loses steepness, with the most notable reduction being from $\beta=1/10$ to

β=1/15. Moreover, wave statistics indicate that the $H_{0.05}$ for the mildest slope is about 38% of that corresponding to the steepest slope (Table 3). This difference varies insignificantly if other parameter combinations, for all Nc values, are analyzed while varying β. These probabilities seem to indicate that, even though there is a clear distinction between β=1/10 and β=1/30 in terms of their tsunami generation potential, the sensitivity of $H_{max}/\Delta h$ to β is rather moderate.

Table 3. Nondimensional $H_{0.05}$ Statistic for a Parameter Space of Variable β

	β = 1/10	β = 1/15	β = 1/20	β = 1/30
$H_{0.05}$	0.0491	0.0344	0.0266	0.0185

Dimensionless Slide Width

In a similar fashion, the width to thickness ratio of the slide will be evaluated by varying its value as indicated in Table 2. The remaining inputs are assigned the following values

$$Nc = 5 \qquad β = 1/20 \qquad doI = 8 \qquad delay = 30$$
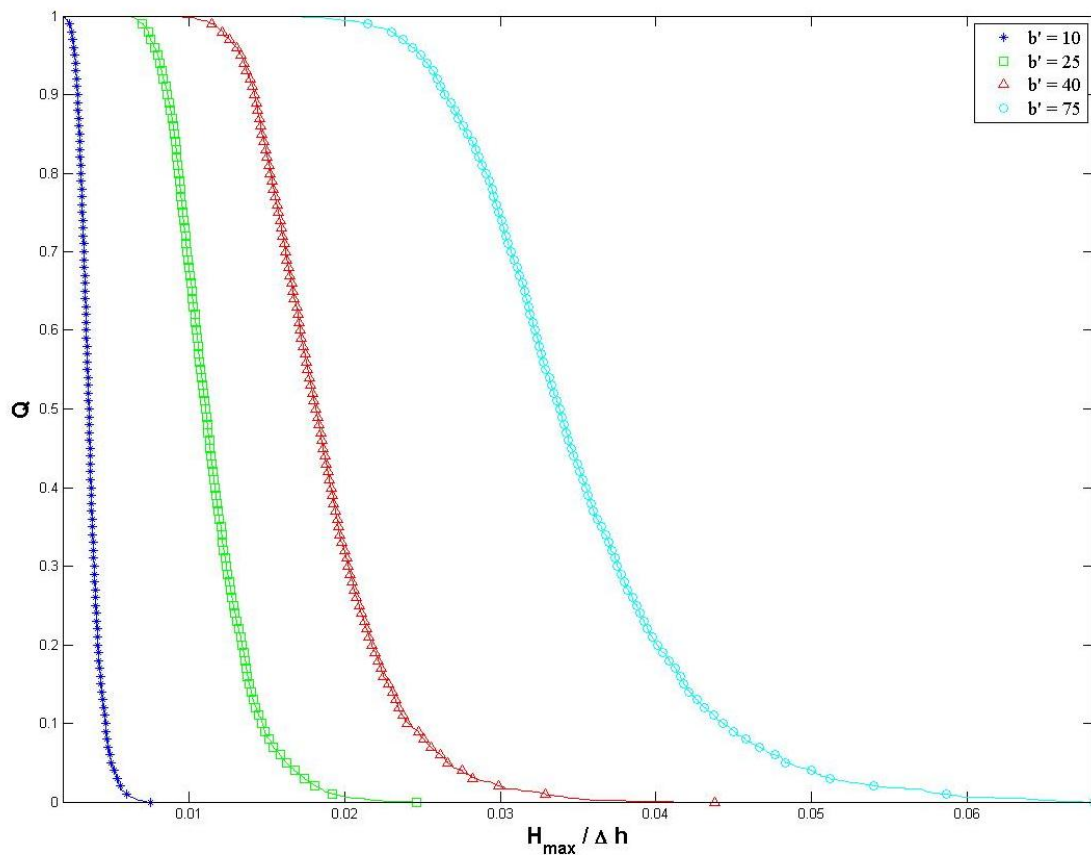
FIG. 15. Probability of Exceedance (*Q*) Curve for Nondimensional Wave Height (*$H_{max}/\Delta h$*) for a Parameter Space with Variable Dimensionless Slide Width (*b'*).

The probability of exceedance for the various *b'* values are shown in Fig. 15. This figure suggests that as *b'* increases, so does the height of the triggered waves. This correlation argues, subsequently, that long, "thin" landslides are the most effective in terms of tsunami generation. In fact, this observation is congruent with *b'* values corresponding to past catastrophic submarine landslides. Hampton et al. (1996) show that the Grand Banks slide, responsible for the worst Canadian tsunami catastrophe, had a *b'* in the order of 303 resulting from a runout length of 110 km and a thickness of 365 m. These slide dimensions resulted, according to Fine et al. 2005, in waves of up to 9 m in height. Hampton et al. (1996) further exemplify, through data corresponding to other major submarine landslide events, that this ratio may be as high as 833 (e.g., Bay of

Biscay slide). The tabulated b' values provided by Hampton et al. (1996), therefore, support the message that Fig. 15 conveys through probability distributions.

Furthermore, Fig. 15 indicates that there is a strong dependency of $H_{max}/\Delta h$ on b'. This can be qualitatively inferred by looking at the significant weakening in the probability distributions as b' becomes small. Examination of $H_{0.05}$ suggests that the smallest b' generates waves that are 10.3% the value of those triggered by $b' = 75$ (Table 4). This percentage is less than one third of that calculated in the sensitivity analysis for β and varies only by about 1% for the higher Nc values and reaches a maximum of 17% for the $Nc = 2$ case. Based on these numbers, b' can be catalogued as a major influential factor in tsunami generation by underwater landslides, which is, in fact, a statement supported by other studies (e.g., Watts 2004).

Table 4. Nondimensional $H_{0.05}$ Statistic for a Parameter Space of Variable b'

	$b' = 10$	$b' = 25$	$b' = 40$	$b' = 75$
$H_{0.05}$	0.00497	0.0162	0.0266	0.0483

Number of Slide Pieces

Parameter Nc will be now investigated with regard to the degree of influence that it possesses on the height of the waves induced by submarine landslides. This investigation will be conducted through probability of exceedance curves for $H_{max}/\Delta h$ as before. The parameter subspace for this analysis consists of the following values

$$\beta = 1/20 \qquad b' = 40 \qquad doI = 8 \qquad delay = 30$$
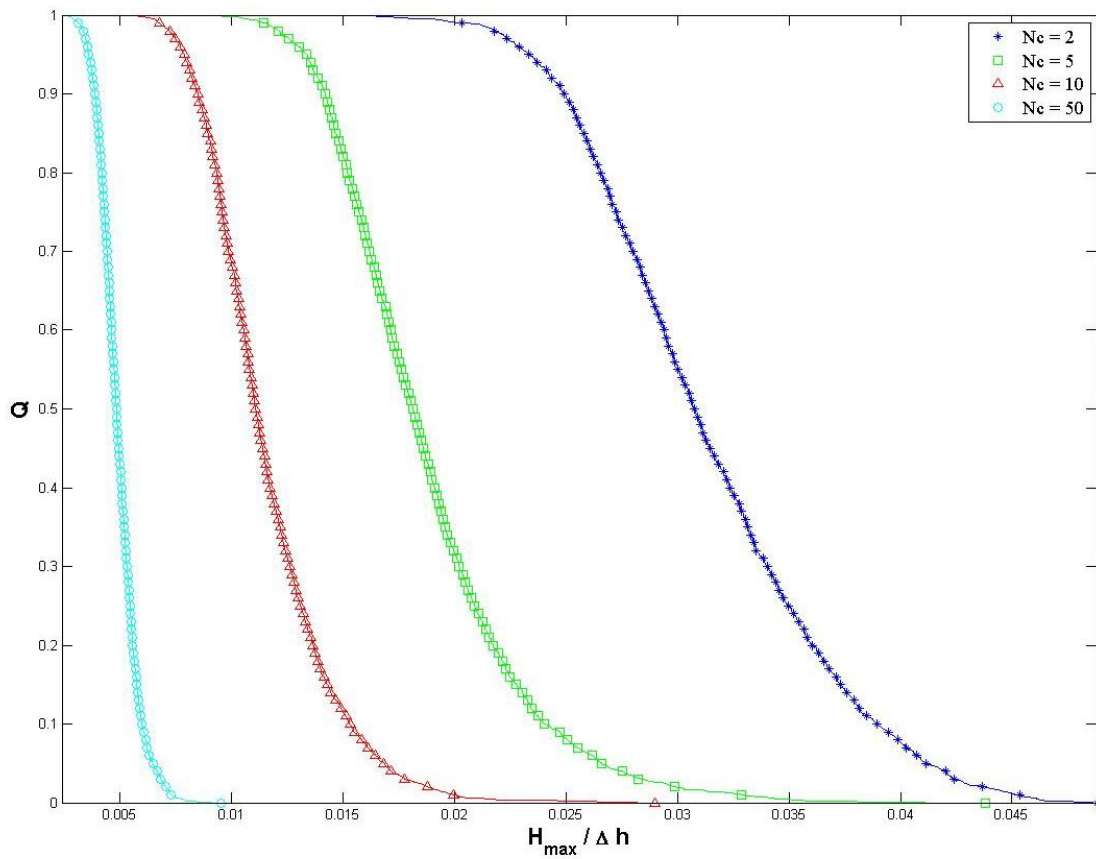
FIG. 16. Probability of Exceedance (*Q*) Curve for Nondimensional Wave Height (*H$_{max}$/Δh*) for a Parameter Space with Variable Number of Slide Pieces (*Nc*).

Table 5. Nondimensional *H$_{0.05}$* Statistic for a Parameter Space of Variable *Nc*

	Nc = 2	*Nc = 5*	*Nc = 10*	*Nc = 50*
H$_{0.05}$	0.0411	0.0266	0.0168	0.0064

As might have been foreseen, the probability of exceedance for any given height is reduced as *Nc* increases. This decrement is more pronounced between the lowest *Nc*

and the one above it magnitude, but it is observed to weaken between adjacent curves from $Nc = 5$ on. The $H_{0.05}$ statistic shows that there is up to a 40% reduction in $H_{max}/\Delta h$ from the $Nc = 2$ to the $Nc = 5$ mode, but only a 20% decrement from the $Nc = 10$ to the $Nc = 50$ scenario (Table 5). These percentages seem to indicate that the sensitivity of $H_{max}/\Delta h$ to Nc decays rapidly as this parameter increases. For $Nc > 10$, in particular, the free surface appears to become remarkably less perceptive to this parameter. Fig. 16 suggests, additionally, that the relation between Nc and $H_{max}/\Delta h$ is reciprocal. In other words, submarine landslides seem to be more effective in transferring energy to the free surface the more they behave as a single mass (i.e., when their Nc is low) when failure occurs. It then would be expected, in this line of reasoning, that the $Nc = 1$ case be associated to the greatest probability of exceedance for a given wave height for the parameter subspace being considered.

The results shown in Fig. 16 as well as the $H_{0.05}$ statistics in Table 5 are found to behave in a similar manner for narrower and wider slides, steeper and milder slopes, shallower and deeper initial depths, and for larger *delay* values. Despite this consistency, an interesting trend is encountered when the value of *delay* is minimized. Fig. 16 argues that the greater the Nc, the smaller the height of the generated waves. However, as *delay* becomes smaller, the slide pieces, despite their number, are forced to move in close proximity to each other, which favors their wave generation potential as they better resemble a one-piece motion. Intuition may suggest that these compact failure modes should approach the probability distribution of the $Nc = 1$ case, if it was available. To prove this reasoning right or wrong, the same parameter subspace used for Fig. 16 will be examined with smaller *delay* values. The results of this examination are shown in Fig. 17 where subplot (a) represents a *delay* value of 5 and subplot (b) a *delay* value of 2.
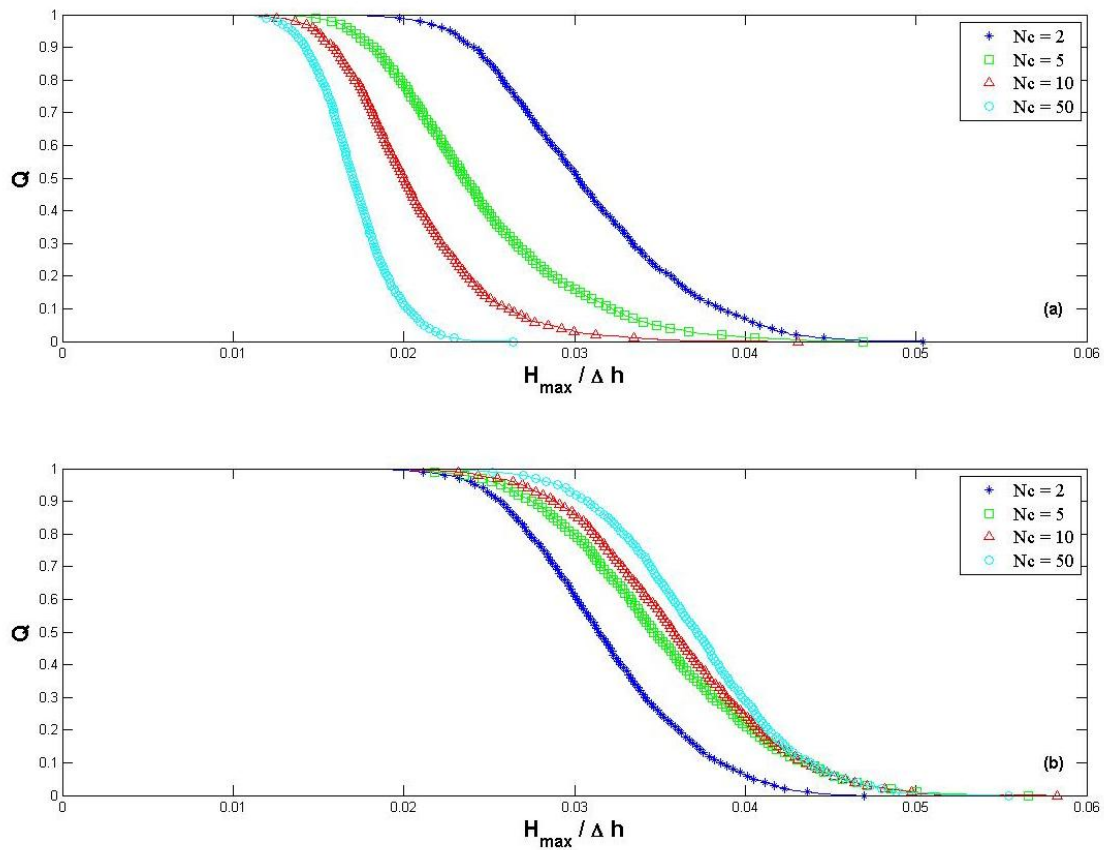
FIG. 17. Probability of Exceedance (*Q*) Curve for Nondimensional Maximum Wave Height ($H_{max}/\Delta h$) for a Parameter Space of Variable Number of Slide Pieces (*Nc*): (a) *delay* = 5, (b) *delay* = 2.

According to Fig. 17a, the tsunami generation potential of the slides with *Nc* = 5, 10 and 50 approaches that of the slide separating into only two pieces as the *delay* value is reduced from 30 (Fig. 16) to 5. Remarkably, when *delay* = 2 (Fig. 17b), the probability distributions undergo a shift where the *Nc* = 50 failure mode now dominates. This shift implies that slide failures involving numerous pieces can accrete their effects on the free surface very efficiently when the overall slide failure is significantly compact. Further examination of Fig. 17b indicates that there is little increase in tsunami generation potential for the *Nc* = 2 case as it transitions from *delay* = 5 to *delay* = 2. This insensitivity is, perhaps, due to the fact that there is still a small time gap between the

first piece to disjoin from the original slide and the second piece to move even when *delay* = 2. Thus, the two slide chunks fail in close proximity, but their effects on the free surface are only partially summed. More importantly, Fig. 17 conveys the impression that the probabilistic relation between *Nc* and $H_{max}/\Delta h$ shifts from being consistently reciprocal to being consistently proportional when *delay* = 2. This then challenges the notion that the single-piece failure is always the most tsunamigenic mode, at least with respect to the shoreward-traveling waves.

Though these observations may seem unexpected at first glance, the fact that a greater *Nc* can be associated to greater exceedance probabilities than a lower *Nc* for very compact failures can be assimilated by examining the Ω values associated to these failure modes. Fig. 18 displays the relation between Ω and $H_{max}/\Delta h$ corresponding to each *Nc* for *delay* = 5 (left panels) and *delay* = 2 (right panels) as well as the minimum Ω values (Ω_{min}) associated to each scenario.
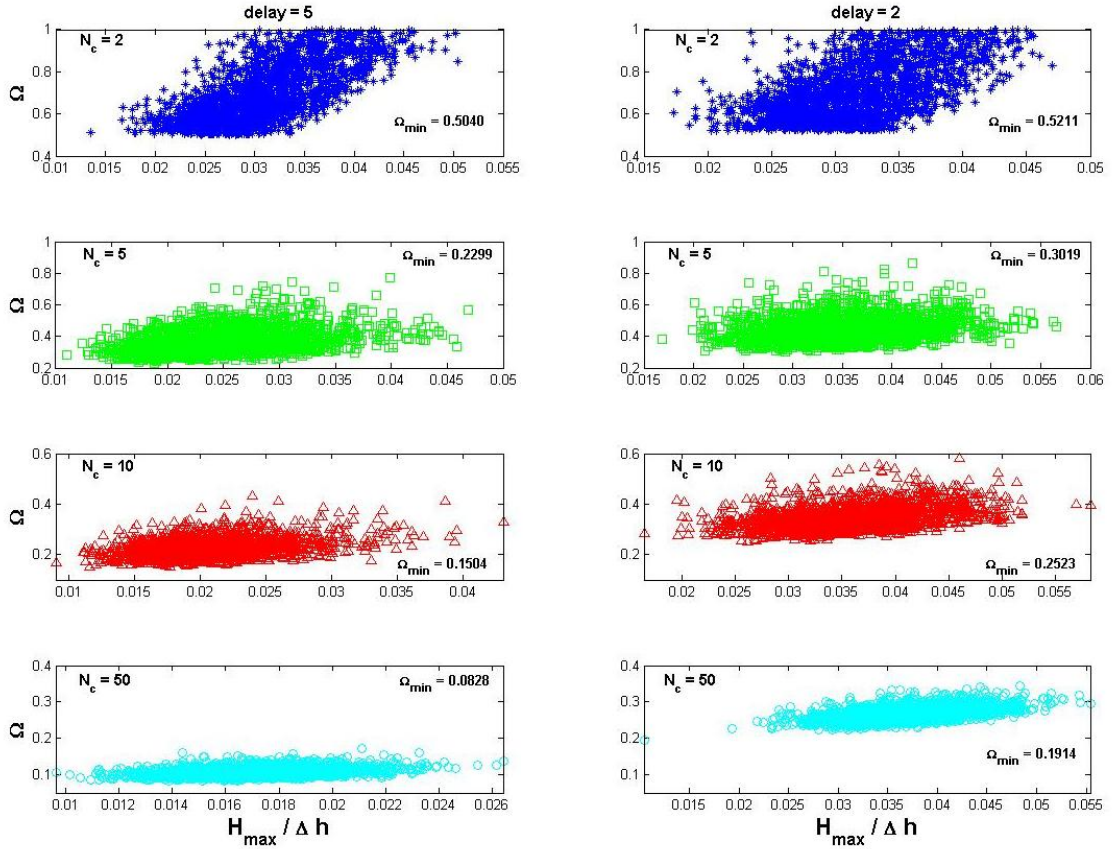
FIG. 18. Slide Coherency (Ω) Versus Nondimensional Maximum Wave Height ($H_{max}/\Delta h$) for a Parameter Space of Variable Number of Slide Pieces (Nc).

Let us recall that Ω refers to the space-time coherency of a given slide. Any reduction in *delay*, therefore, automatically induces increments in Ω because the slide pieces move in closer proximity to each other. Hence, it is no surprise that each of the Nc cases shown in Fig. 18 experiences an increase in their Ω_{min} from left panel to right panel. Moreover, any increase in Nc is accompanied by a reduction in Ω because the slide is departing from behaving like a single-piece slide. Thus, the decrements in Ω observed in Fig. 18 as Nc increases are consistent with the definition of this variable. It is conceivable, therefore, that a special case results as *delay* becomes considerably small and Nc large because, although in space the slide is diverting from a single-piece

configuration, the start motion times of each slide chunk are extremely close to each other, causing the overall failure to acquire a very compact appearance. In this context, the Nc = 50 case experiences the greatest increase in Ω_{min} from left to right panel because the start motion times of all 50 pieces are tightly confined, forcing these entities to move virtually simultaneously. According to Fig. 18, this gain in Ω is then reflected in an increment in tsunami generation potential. Hence, slide failures of low spatial coherency and very compact temporal features impart a greater amount of energy to the free surface than more spatially coherent failure modes. Based on this proposition, the Nc = 1 mode does not possess the greatest tsunami generation potential when compared to extremely compact failures involving numerous slide pieces.

A point that has arisen from this discussion concerns the prediction of the probability distributions for other Nc values (e.g., Nc = 1, 3, 100) in the context of very compact failures. Evaluation of other Nc values would help to confirm the proposition of Figs. 17 and 18 that numerous slide pieces may manifest a greater potential to disturb the free surface, when triggered closely together, than a low Nc failure mode. Single simulations conducted for the Nc = 1 case, however, do confirm that the waves observed above the rear of the landslide are smaller in height than those induced by larger Nc values when *delay* = 2. Nonetheless, any other *delay* value produces probability distributions that exhibit a reciprocal relation between Nc and $H_{max}/\Delta h$ such as that shown in Fig. 16.

Wanting to explore the influence of parameter Nc in more detail when small *delay* values occur, the probability distributions of all four *b'* in Table 2 were inspected to analyze the behavior of these compact failures as the size of the initial slide varies. Figs. 19 and 20 contain the results of these examinations.
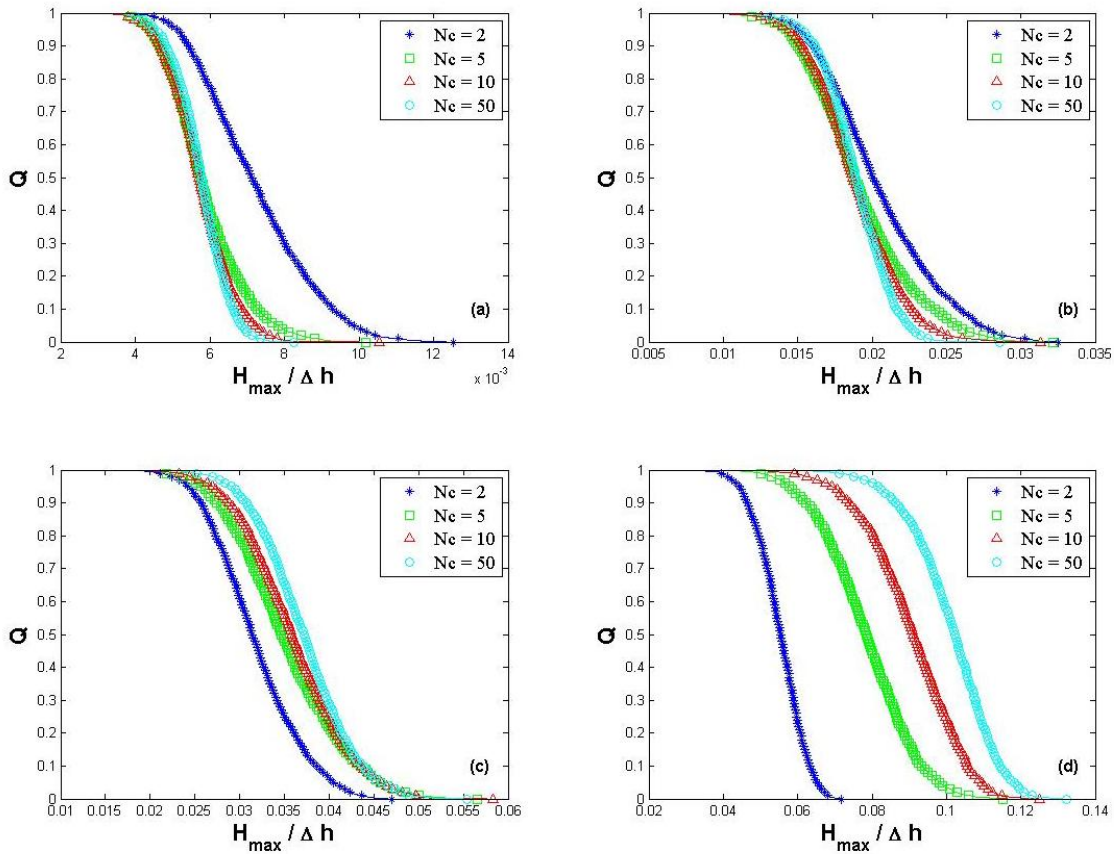
FIG. 19. Probability of Exceedance (*Q*) Curve for Nondimensional Maximum Wave Height ($H_{max}/\Delta h$) for Parameter Spaces of Variable Number of Slide Pieces and *delay* = 2: (a) *b'* = 10, (b) *b'* = 25, (c) *b'* = 40, (d) *b'* = 75.

By displaying the results obtained for all *b'* for the available *Nc* values, Fig. 19 suggests that the shift in wave generation potential when *delay* = 2 does not occur for all the scenarios contemplated in the parameter space defined by Table 2. Based on Figs. 19a and 19b, slides with *b'* ≤ 25 do not manifest the shifting behavior, conveying that the size of the slide pieces has a greater impact on the free surface response than the degree of compactness of the overall failure. Fig. 18b, however, gives evidence that *b'* = 25 is close to the point where the extent of failure compaction starts to play a role. Furthermore, panels (c) and (d) in Fig. 18 point out that as slide width increases, the failure modes with greater *Nc* begin to overcome, in terms of tsunami generation

potential, the lower Nc modes. This is more prominent for $b' = 75$ where the shifting behavior for *delay* = 5 (not shown here) is also exhibited. It would be reasonable to say, based on Figs. 19c and 19d, that when the slide becomes sufficiently long, the size of the individual pieces becomes secondary and the temporal compactness of the failure primary. Notice, however, that the waves do acquire a greater height as b' increases regardless of the value of Nc. This is congruent with what was found in the sensitivity analysis of b'.

Given the conduct of the results just discussed, the next intuitive step is to explore the probability distributions of the waves propagating away from the coast in order to generalize or restrict the propositions of Figs. 17 - 20. Below, Fig. 20 shows the probability of exceedance for $H_{max}/\Delta h$ corresponding to a location on the free surface above the slide front (Fig. 20a) and offshore (Fig. 20b) from the initial slide position. Moreover, these results correspond to a slide that has the largest b' and smallest *delay* in Table 2. The rest of the subspace parameters remain unchanged.
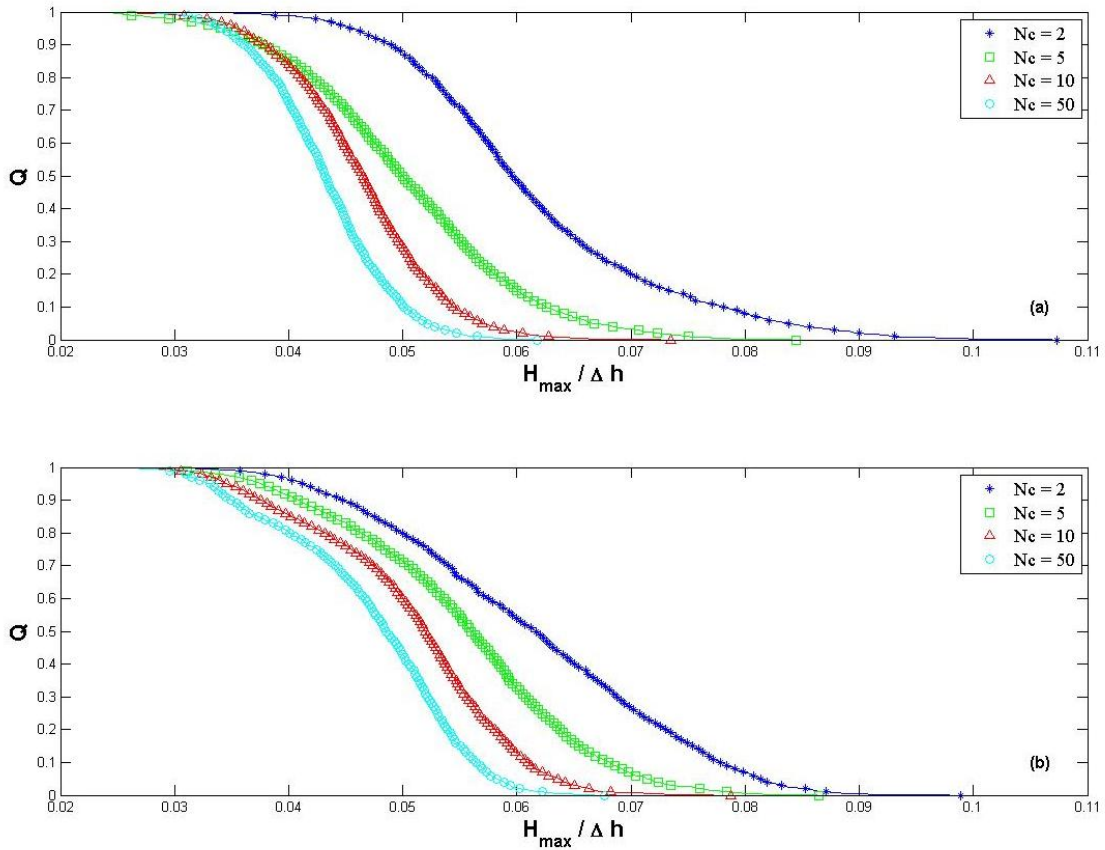
FIG. 20. Probability of Exceedance (*Q*) Curve for Nondimensional Maximum Wave Height ($H_{max}/\Delta h$) for Variable *Nc* with *b'* = 75 and *delay* = 2: (a) Above Slide Front, (b) Offshore Location.

The waves traveling in the offshore direction appear to behave differently, in general, according to Fig. 20. Although *delay* has been reduced to its minimum and *b'* given its maximum, the correlation between *Nc* and $H_{max}/\Delta h$ does not change for either the location above the slide front (Fig. 20a), nor the location farthest offshore (Fig. 20b). The offshore-propagating waves, therefore, show a consistent pattern which supports the notion that the size of the waves increases as *Nc* decreases. This fact, perhaps, fulfills the more intuitive reasoning with which the sensitivity analysis for parameter *Nc* commenced. Fig. 20 further argues that wave generation potential in the location of the

slide front is primarily determined by the size of the detached slide chunks rather than on the degree of compaction of the overall failure. Although this group of results will not be any further discussed, the probability distributions for the offshore field could also serve to assess the hazard posed by submarine landslides to offshore assets located in areas of high seafloor environmental loading.

Nondimensional Initial Slide Depth

The contribution of parameter *doI* to the height of submarine landslide-induced waves will be next tested. The constant parameters are defined as follows

$$Nc = 5 \qquad \beta = 1/20 \qquad b' = 40 \qquad delay = 30$$

Fig. 21 shows the results of this evaluation condensed in the form of probability of exceedance distributions. Not surprisingly, the deeper the water depth at which the slide starts moving, the lesser the degree at which the free surface is disturbed. An interesting deduction from Fig. 21 is that the difference in $H_{max}/\Delta h$ between *doI* = 5 and *doI* = 8 is considerable, but the height of the waves generated by the largest and intermediate *doI* values are comparable. Moreover, Table 6 indicates that $H_{0.05}$ for the largest *doI* is about 46% the magnitude of that corresponding to the shallowest depth. In general, the sensitivity of $H_{max}/\Delta h$ to *doI* is observed to be moderate and the weakest one so far explored. Be mindful, however, that *doI* is also the most restricted parameter due to the required full slide submergence, the defective right open boundary, and the points of interest on the free surface.
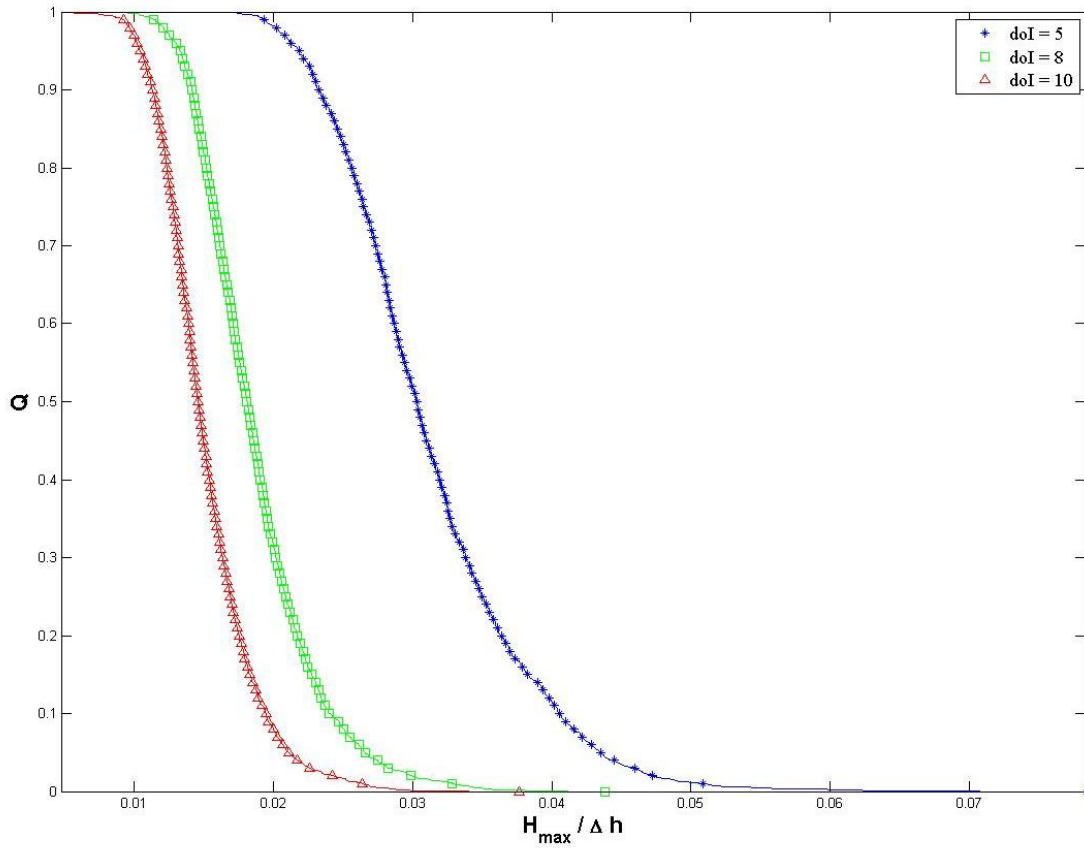
FIG. 21. Probability of Exceedance (*Q*) Curve for Nondimensional Wave Height (*H_max/Δh*) for a Parameter Space with Variable Dimensionless Slide Initial Depth (*doI*).

Table 6. Nondimensional $H_{0.05}$ Statistic for a Parameter Space of Variable *doI*

	doI = 5	*doI = 8*	*doI = 10*
$H_{0.05}$	0.0435	0.0266	0.0211

Dimensionless Slide Failure Delay

To finalize the sensitivity analysis, the parameter which is involved in the computation of the start motion time of a slide piece will be evaluated. The constant parameters are

$$Nc = 5 \qquad \beta = 1/20 \qquad b' = 40 \qquad doI = 8$$
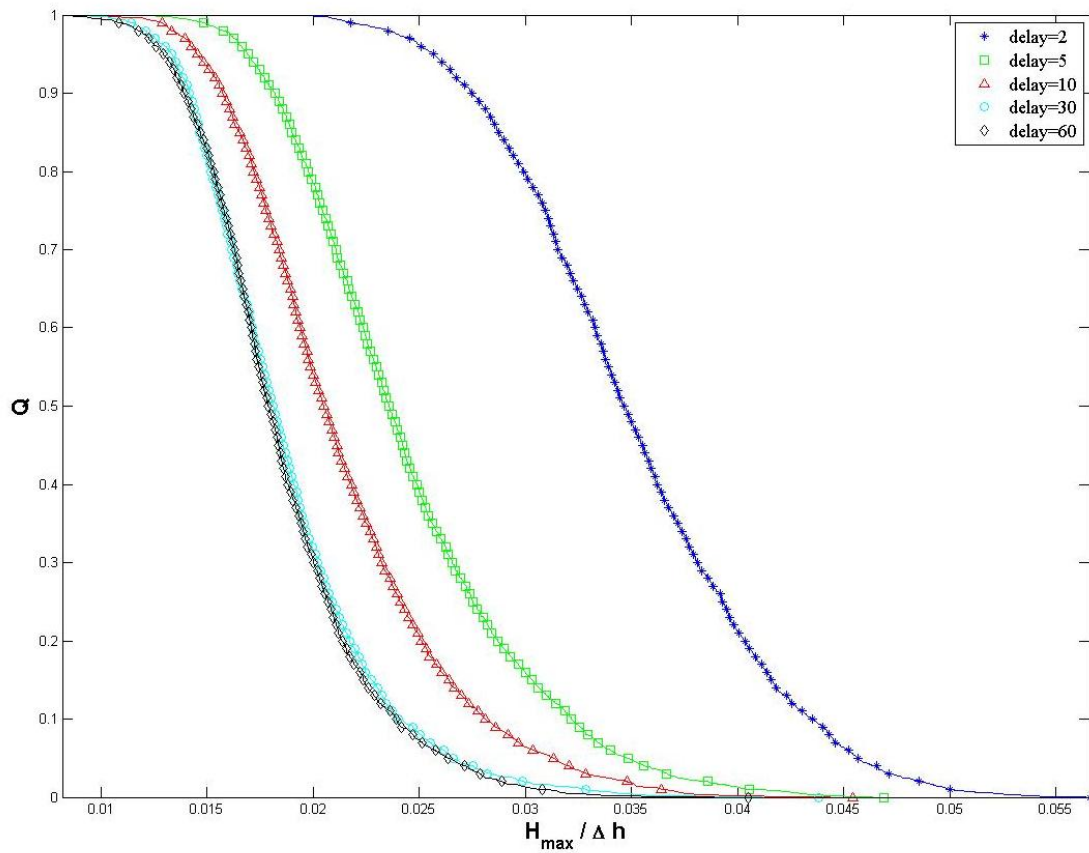
FIG. 22. Probability of Exceedance (Q) Curve for Nondimensional Wave Height ($H_{max}/\Delta h$) for a Parameter Space with Variable Dimensionless Slide Failure Delay (*delay*).

In agreement with the meaning of *delay*, Fig. 22 demonstrates that as the gap between the start motion times of the slide pieces is compressed, the energy transfer from each individual failure is better accreted and wave generation potential is favored. It is also appreciable in Fig. 22 that there is a pronounced difference between the minimum *delay* value and the following one, suggesting that the coupling with the free surface considerably debilitates in this transition. This weakening is in the order of 30% in terms of the $H_{0.05}$ statistic. In spite of this, there is only a moderate reduction in $H_{max}/\Delta h$ as *delay* continues to increase. Notice, too, that the biggest *delay* and the one below it in magnitude almost perfectly overlap their distributions. Hence, *delay* values greater than 60 are not expected to deviate much from the leftmost distributions in Fig. 22. In general, Fig. 22 argues that the tsunami generation potential of separable submarine landslides rapidly decays as the slide pieces in which it fails reduce their degree of interaction.

Table 7. Nondimensional $H_{0.05}$ Statistic for a Parameter Space of Variable *delay*

	delay = 2	*delay = 5*	*delay = 10*	*delay = 30*	*delay = 60*
$H_{0.05}$	0.0456	0.0348	0.0313	0.0266	0.0263

Discussion

Although only one parameter subspace was considered, the outcome of the sensitivity analysis provides valuable insight regarding the influence of the various parameters on tsunami generation by submarine landslides. By inspecting the gathered statistics for $H_{0.05}$, a modest parameter rank of dominancy can be established. The order of this rank is not determined based on the highest $H_{0.05}$ recorded, but on the degree to which this wave statistic fluctuates with parameter variations. In this context, the most

influential parameter corresponds to *b'*. This input was observed to drive changes of similar weight in the dimensionless height of the waves for all its discrete values. Next in the rank is parameter *Nc*. The effect of this parameter on the free surface response was valued as significant, but also observed to considerably debilitate for values greater than 10. Third in the list is parameter β. This input was observed to be most influential in computing a_o, but only moderately important in the resulting dimensionless wave heights. Parameter *doI* succeeds in the rank, although its impact on tsunami generation potential was discerned to be fairly similar to β. Recall, however, that *doI* was the most restricted parameter in terms of the values that were designated to it. Among the deterministic parameters, *delay* demonstrated to be the weakest driver of the $H_{0.05}$ statistic. This is mainly because its impact highly weakens as its value enlarges. Nonetheless, small *delay* values were observed to notably contribute to tsunami generation. Finally, parameters γ and C_m manifested a notable influence on the magnitude of a_o; however, their contribution to the free surface response was only discerned for some data points where Ω was disproportional to $H_{max}/\Delta h$.

The various probability distributions that have been constructed during the sensitivity analysis of each input parameter indicate that the hazard that tsunamis induced by submarine landslides pose to the coast may be significant in some cases. The various tables containing the values of $H_{0.05}$ which were drawn from the probability distributions of each parameter convey that $H_{0.05}$ close to 0.05 may be attained with the selected parameter subspace. For this combination of attributes to be tsunamigenic, therefore, the landslide must be substantially thick. Hampton et al. (1996), however, show that, for example, a typical submarine landslide in the Atlantic Ocean can attain a thickness in the order of 1200 m. With these figures in mind, it is easy to value the hazard that submarine landslides may pose to the coast when their features and those of the local environment favor their tsunami generation potential. It is indisputably important, thereby, to devise tools, such as this probabilistic model, to estimate this risk.

CHAPTER VII

CONCLUSIONS

A numerical study of the tsunamis induced by the translational failure of submarine rigid landslides has been conducted. Given the dispersive behavior of this specific type of waves, a fully dispersive MSE model for small amplitude waves was recreated using a finite-difference scheme and satisfactorily validated. This model is equipped with a filter function that mimics the effects of the water column above the landslide and favors the reproduction of long waves. Except for a boundary issue, the recreated model performed remarkably well, offering good accuracy, excellent reproduction of dispersion effects, and low computational cost in its 1-D version. Despite its incapability to account for nonlinear effects and abrupt bottom changes, the linear MSE model proved to be adequate for the modeling of tsunami generation and propagation in the context of underwater ground motion.

In order to amplify what has been covered in the past with regard to submarine landslide tsunamis, the presented model incorporated the concept of underwater slides whose failure is characterized by the separation of a user-defined number of rigid pieces. The centers of mass motion of these detached slides was computed using the equations of Watts (1998) which describe rigid bodies that translate down a flat slope with a decaying acceleration until a terminal velocity is reached. The free surface response to this ground motion was observed to conform to the wave forms of submarine landslide tsunamis described in previous studies.

An ad-hoc formulation for landslide coherency was developed with the purpose of describing the spatial and temporal characteristics of the overall slide failure. This expression relates the size and start motion times of each slide piece to provide insight on the compactness of the failure of the landslide. The results obtained with the completion of the study indicated that the proposed formulation was an excellent indicator of not only failure progression, but also of the extent to which the detached

slide pieces combine their effect on the free surface. In general, the presented expression for coherency suggested that landslide failures increase their tsunamigenic potential the closer they behave to the single-slide motion.

Aiming at probabilistically studying the hazard posed by these tsunami-generating mechanisms, a Monte Carlo method was adopted in which deterministic and probabilistic parameters were defined in the form of parameter spaces and normal distributions, respectively. The Monte Carlo simulations consisted of 2000 trials that captured the number, period and height of the generated waves at different locations above the landslide and at an offshore point of interest through zero-up crossing analysis. The emphasis in this study, however, was given to the shoreward traveling waves generated above the rear of the landslide. The Monte Carlo methodology proved to be adequate to examine the behavior of the multiple independent slide parameters, providing consistent results in the form of probability distributions for the maximum recorded wave height.

In agreement with the general conception found in the literature, the results of the Monte Carlo simulations are suggestive that tsunamis generated by submarine landslides are strongly a function of the attributes of the source, the ocean bottom, and the dynamics of the moving mass. Attempting to recognize the extent at which these failure aspects control tsunami generation, a sensitivity analysis for the deterministic parameters was conducted. Based on wave statistics extracted from probability of exceedance distributions, the sensitivity analysis pointed out that b' and Nc are the most influential parameters, followed by β, *doI*, and *delay*. With regard to parameter b', it was found that long, "thin" landslides exhibit an effective tsunami generation potential, which is in agreement with estimates of b' values for past historic events. Parameters C_m, γ, and C_d were observed to affect the magnitude of a_o, but to be dominated by the influence of the other parameters in their contribution to the height of the generated waves.

The introduction of the concept of submarine landslides breaking into smaller pieces as failure unfolds had a significant impact on the outcome of the simulations. For most of the cases contemplated, it was found that underwater landslides become

considerably less tsunamigenic when they separate into smaller, numerous pieces. A sensitivity analysis conveyed that the free surface becomes progressively imperceptive to these multi-slide failures as the number of pieces involved in the failure grows. The only exception to these findings applies to very compact failures where the slide pieces move almost simultaneously. In this type of failure modes, the confined triggering of the numerous pieces was observed to create a coupling with the free surface greater than more spatially coherent slides. This behavior seems to be further enhanced as the slide is enlarged. In view of these observations, the case in which the slide moves as one piece is not always the mode with the highest tsunami generation potential. This argument only holds, however, for the waves propagating in the direction of the shore.

A quick evaluation of the wave data collected above the slide front and at the offshore location was also conducted. The offshore-traveling waves appeared to consistently increase in height as the slide approaches the one-piece motion. This then is suggestive that energy transfer to the free surface varies depending on the location above the slide being examined. Further investigation of the waves propagating away from the coast could be beneficial to estimate submarine landslide tsunami hazard for offshore assets.

The presented results also provided valuable insight on the overall hazard posed by submarine landslides. Previous probabilistic studies have labeled this hazard as low, in large part due to their focus on specific geographical regions. The results of this study are representative of a hazard of rather low character, but that can significantly escalate its potential when a favorable combination of physical attributes and failure compactness of the submarine landslide occur. Recall, also, that the presented hazard assessment does not account for the nonlinear processes or wave focusing effects that will certainly act on the tsunami as it reaches the coast. Nevertheless, this study does provide new insight on the general perception of submarine landslide tsunamis and their unquestionable threat to the coast.

.

Recommendations for Future Research

In the context of modeling the generation and propagation of submarine landslide tsunamis using a linear model, the fully dispersive MSE model is certainly an adequate vehicle. In spite of this, the radiation condition imposed on the right open boundary exhibited a defective behavior in the form of reflected waves as the slide left the domain. This issue had negative consequences in the implementation of the Monte Carlo simulations because the domain had to be significantly extended to capture a sufficiently long time series before the reflected waves could contaminate the results. With the extension of the domain, of course, came the need to use a coarser grid that, subsequently, decreased the accuracy of the results. Therefore, correcting the behavior of this boundary would be a very meaningful improvement to this model as the number of trials per Monte Carlo sequence could be increased and a more accurate and robust hazard assessment performed.

Another improvement suggested for this model is to assign more adequate standard deviation values to the normal distributions of C_m, γ, and C_d. Perhaps, focusing the study on a particular geographical area will narrow the range of values that can be assigned to these parameters. In addition, ways of randomizing some of the deterministic parameters, such as *delay*, could be explored.

Extension of the probabilistic study to 2-D is also recommended. Revision of the 2-D MSE model here evaluated is crucial in order to look for improvements in the reconstruction of the free surface near the generation region. Moreover, a 2-D study would allow for the examination of 3-D effects and their impact on the characteristic of the triggered tsunamis. In particular, the study of the 2-D behavior of the very compact failure modes that were of intriguing nature in this study is highlighted.

The hazard assessment here conducted was restricted to the parameter space utilized in the Monte Carlo simulations. A more robust assessment would allow for the prediction of wave statistics (e.g., $H_{0.05}$) through calibrated expressions involving the various slide parameters. This approach is well exemplified by Lynett and Liu (2005)

who developed expressions for the run-up provoked by 3-D submarine and subaerial landslides. Expansion of the presented hazard assessment, therefore, should be inclined towards developing such expressions. The author certainly hopes to be able to implement this idea in the near future.

REFERENCES

Abadie, S., Morichon, D., Grilli, S., and Glockner, S. (2010). "Numerical simulation of waves generated by landslides using a multiple-fluid Navier-Stokes model." *Coastal Engrg.*, 57, 779 – 794.

Almagor, G. (1982). "Marine geotechnical studies at continental margins: A review – Part II". *Appl. Ocean Res.*, 4(3), 130 – 150.

Assier Rzadkiewicz, S., Mariotti, C., Heinrich, P. (1997). "Numerical simulation of submarine landslides and their hydraulic effect." *J. Wtrwy., Port, Coast, and Oc. Engrg.*, ASCE, 123(4), 149 – 157.

Bellotti, G., Cecioni, C., and De Girolamo, P. (2008). "Simulation of small-amplitude frequency-dispersive transient waves by means of the mild-slope equation." *Coastal Engrg.* 55, 447 – 458.

Biscontin, G., Pestana, J.M., and Nadim, F. (2004). "Seismic triggering of submarine slides in soft cohesive soil deposits." *Marine Geology*, 203, 341 – 354.

Booth, J.S., O′ Leary, D.W., Popenoe, P., and Danforth, W.W. (2002). "U.S. Atlantic continental slope landslides: Their distribution, general attributes, and implications." *Submarine landslides: Selected studies in the U.S. Exclusive Economic Zone*, Edited by W.C. Schwab, H.J. Lee, and D.C. Twichell, 14 – 22.

Borrero, J.C., Okal, E.A., and Synolakis, C.E. (2002). "Solving the puzzle of the 1998 Papua New Guinea tsunami: The case for a slump." *Solutions to Coastal Disasters*, Edited by L. Wallendorf, and L. Ewing, Amer. Soc. Civil Eng., 863 – 877.

Blevins, R.D. (1984). *Applied fluid dynamics handbook*. Van Nostrand Reinhold, New York, NY.

Brocchini, M. and Dodd, N. (2008). "Nonlinear Shallow Water Equation Modeling for Coastal Engineering." *J. Wtrwy., Port, Coast, and Oc. Engrg.*, ASCE, 134(2), 104 – 120.

Cecioni, C. and Bellotti, G. (2010a). "Modeling tsunamis generated by submerged landslides using depth integrated equations." *Appl. Ocean Res.*, 32(3), 343 – 350.

Cecioni, C. and Bellotti, G. (2010b). "Inclusion of landslide tsunamis generation into a depth integrated wave model." *Nat. Hazards Earth Syst. Sci.*, 10, 2259 – 2268.

Chaytor, J.D., ten Brink, U.S., Solow, A.R., and Andrews, B.D. (2009). "Size distribution of submarine-landslides along the U.S. Atlantic margin." *Marine Geology*, 264, 16 – 27.

Demirbilek, Z. and Panchang, V. (1998). "CGWAVE: A coastal surface water wave model of the mild slope equation." *Technical Report*, U.S. Army Engineer Research and Development Center (ERDC), Vicksburg, MS, 1998.

Dingemans, M.W. (1997). *Water wave propagation over uneven bottoms,* World Scientific, Singapore.

Enet, F., Grilli, S. T., and Watts, P. (2003). "Laboratory experiments for tsunamis generated by underwater landslides: Comparison with numerical modeling." *Proc., 13th Offshore and Polar Engineering Conf., Intl. Soc. of Offshore and Polar Engineers*, Cupertino, Calif., 3, 372–379.

Enet, F., and Grilli, S. T. (2005). "Tsunami landslide generation: Modeling and experiments." *Proc., 5th Int. on Ocean Wave Measurement and Analysis, WAVES 2005*, Madrid, Spain, IAHR, Paper No. 88.

Enet, F. and Grilli, S.T. (2007). "Experimental study of tsunami generation by three-dimensional rigid underwater landslides." *J. Wtrwy., Port, Coast, and Oc. Engrg.*, ASCE, 133(6), 442 – 454.

Fenton, J.D. and McKee, W.D. (1990). "On calculating the lengths of water waves". *Coastal Engrg.*, 14, 499 – 513.

Fine, IV., Rabinovich, A.B., Bornhold, B.D., Thomson, R.E., and Kulikov, E.A. (2005). "The Grand Banks landslide-generated tsunami of November 18, 1929: Preliminary analysis and numerical modeling." *Marine Geology*, 215, 45 – 57.

Fritz, H.M., Hager, W.H., and Minor, H.-E. (2004). "Near field characteristics of landslide generated impulse waves." *J. Wtrwy., Port, Coast, and Oc. Engrg.*, ASCE, 130(6), 287 – 302.

Fructus, D. and Grue, J. (2007). "An explicit method for the nonlinear interaction between water waves and variable and moving bottom topography." *J. Computational Physics*, 222, 720 – 739.

Fuhrman, D.R. and Madsen, P.A. (2009). "Tsunami generation, propagation, and run-up with a high-order Boussinesq model." *Coastal Engrg.*, 56, 747 – 758.

Geist, E.L. and Parsons, T. (2006). "Probabilistic analysis of tsunami hazards." *Natural Hazards*, 37, 277 – 314.

Grilli, S.T. and Watts, P. (1999). "Modeling of waves by a moving submerged body. Applications to underwater landslides." *Engrg. Anal. Bound. Elem.*, 23, 645 – 656.

Grilli, S.T. and Watts, P. (2005). "Tsunami generation by submarine mass failures I: Modeling, experimental validation, and sensitivity analysis." *J. Wtrwy., Port, Coast, and Oc. Engrg.*, ASCE, 131(6), 283 – 297.

Grilli, S.T., Taylor, O.S., Baxter, C.D.P., Maretzki, S. (2009). "A probabilistic approach for determining submarine landslide tsunami hazard along the upper east coast of the United States." *Marine Geology*, 264, 74 – 97.

Hammack, J.L. (1973). "A note on tsunamis: Their generation and propagation in an ocean of uniform depth." *J. Fluid Mech.*, 60, 769 – 799.

Hampton, M.A., Lee, H.J., and Locat, J. (1996). "Submarine Landslides." *Review of Geophysics*, 34, 33 – 59.

Harbitz, C.B. (1992). "Modeling simulations of tsunamis generated by the Storegga slides." *Marine Geology*, 105, 1 – 21.

Harbitz, C.B., Pedersen, G., Gjevik, B. (1993). "Numerical simulation of large water waves due to landslides." *J. Hydraul. Div.*, ASCE, 119(12), 1325 – 1342.

Hienrich, P. (1992). "Nonlinear water waves generated by submarine and aerial landslides." *J. Wtrwy., Port, Coast, and Oc. Engrg.*, ASCE, 118(3), 249 – 266.

Hienrich, P., Piatanesi, A., and Hebert, H. (2001). "Numerical modeling of tsunami generation and propagation from submarine slumps: The 1998 PNG events." *Geophys. J. Int.,* 145, 97 – 111

Hirt, C.W., and Nichols, B.D. (1981). "Volume of Fluid (VOF) method for the dynamics of free boundaries." *J. Computational Physics*, 39, 201 – 225.

Imamura, F. and Imteaz, M.M.A. (1995). "Long waves in two layers: Governing equations and numerical model." *Sci. Tsunami Hazards*, 14, 13 – 28.

Iwasaki, S. (1982). "Experimental study of a tsunami generated by a horizontal motion of a sloping bottom." *Bull. Earth. Res. Inst.*, 57, 239-262.

Kervella, Y., Dutykh, D., and Dias, F. (2007). "Comparison between three-dimensional linear and nonlinear tsunami generation models." *Theor. Comput. Fluid Dyn.*, 21, 245 – 269.

Jiang, L., and LeBlond, P.H. (1992). "The coupling of a submarine slide and the surface waves which it generates." *J. Geophys. Res.*, 97(C8), 12,731 – 12,744.

Jiang, L., and LeBlond, P.H. (1993). "Numerical modeling of an underwater Bingham plastic mudslide and the waves which it generates." *J. Geophys. Res.*, 98(C6), 10,303 – 10,317.

Lee, H.J., Schwab, W.C., and Booth, J.S. (2002). "Submarine landslides: An introduction." *Submarine landslides: Selected studies in the U.S. Exclusive Economic Zone*. Edited by W.C. Schwab, H.J. Lee, & D.C. Twichell, 1 – 13.

Lin, P. (2011). "Numerical modeling of water waves." Ocean Engineering Seminar, Texas A&M University.

Liu, P.L.F., Wu, T.R., Raichlen, F., Synolakis, C.E., Borrero, J.C. (2005). "Runup and drawdown generated by three-dimensional sliding masses." *J. Fluid Mech.*, 536, 107 – 144.

Lopez-Venegas, A.M., ten Brink, U.S., and Geist, E.L. (2008). "Submarine landslide as the source for the October 11, 1918 Mona Passage tsunami: Observations and modeling." *Marine Geology*, 254, 35 – 46.

Lynett, P.J. and Liu, P.L.F. (2002). "A numerical study of submarine-landslide-generated waves and run-up." *P. Roy. Soc. London*, 458, 2885 – 2910.

Lynett, P.J. and Liu, P.L.F. (2005). "A numerical study of the run-up generated by three-dimensional landslides." *J. Geophys. Res.*, 110(C03006), doi:10.1029/2004JC002443.

Lynett, P.J., Borrero, J.C., Liu, P.L. and Synolakis, C.E. (2003). "Field survey and numerical simulations: A review of the 1998 Papua New Guinea tsunami." *Pure and Applied Geophysics*, 160, 2119 – 2146.

Maretzki, S., Grilli, S.T., and Baxter, C.D.P. (2007). "Probabilistic SMF tsunami hazard assessment for the upper East Coast of the United States.". *Proc., 3rd Intl. Symp. on Submarine Mass Movements and their Consequences,* Edited by V. Lykousis, D. Sakellariou, and J. Locat, Springer, 377 – 386.

Murray, R. J. (1989). "Short wave modelling using new equations of Boussinesq type." *Proc., 9th Australasian Conf. on Coast. and Oc. Engrg.,* Institution of Engineers, Adelaide, Australia, 331 – 336.

McAdoo, B.G., Pratson, L.F., and Orange, L.F. (2000). "Submarine landslide geomorphology, US continental slope." *Marine Geology*, 169, 103 – 136.

National Geophysical Data Center / World Data Center (NGDC/WDC) Historical Tsunami Database, Boulder, CO, USA. (Available at http://www.ngdc.noaa.gov/hazard/tsu_db.shtml).

Nwogu, O. (1993). "Alternative form of Boussinesq equations for nearshore wave propagation." *J. Wtrwy., Port, Coast, and Oc. Engrg.*, ASCE, 119(6), 618 – 638.

Pelinovsky, E. and Poplavsky, A. (1996). "Simplified model of tsunami generation by submarine landslides." *Phys. Chem. Earth*, 21(12), 13 – 17.

Peregrine, D.H. (1967). "Long waves on a beach." *J. Fluid Mech.*, 27, 815 – 827.

Press, W.H., Teokolsky, S.A., Vetterling, W.T., Flannery, B.P. (1992). *Numerical recipes in FORTRAN 90: The art of scientific computing*. Cambridge University Press, New York, NY.

Raney, D.C. and Butler, H.L. (1976). "Landslide generated water wave model." *J. Hydraul. Div.*, ASCE, 102(9), 1269 – 1282.

Synolakis, C.E., Bardet, J., Borrero, J.C., Davies, H.L., Okal, E.A., Silver, E.A., Sweet, S., and Tappin, D.R. (2002). "The slump origin of the 1998 Papua New Guinea tsunami." *Proc. R. Soc. Lond. A*, 458, 763-789.

Synolakis, C. E., and Raichlen, F. (2003). "Waves and runup generated by a three-dimensional sliding mass." *Submarine mass movements and their consequences*, Edited by J. Locat and J. Mienert, Klüwer Academic, Dordrecht, The Netherlands, 113 – 119.

Tappin, D.R. (2010). "Submarine mass failures as tsunami sources: Their climate control." *Phil. Trans. R. Soc. A*, 368, 2417 – 2434.

Tinti, S., Pagnoni, G., and Zaniboni, F. (2006). "The landslides and tsunamis of the 30th of December 2002 in Stromboli analyzed through numerical simulations." *Bulletin of Volcanology* 68 (5), 462 – 479.

Ward, (2001). S.N. "Landside tsunami." *J. Geophys. Res.*, 106(6),11,201 – 11,215.

Watts, P. (1998). "Wavemaker curves for tsunamis generated by underwater landslides." *J. Wtrwy., Port, Coast, and Oc. Engrg.*, ASCE, 124(3), 127 – 137.

Watts, P. (2000). "Tsunami features of solid block underwater landslides." *J. Wtrwy., Port, Coast, and Oc. Engrg.*, ASCE, 126(3), 144 – 152.

Watts, P., Imamura, F., and Grilli, S. T. (2000). "Comparing model simulations of three benchmark tsunami generation cases." *Sci. Tsunami Hazards*, 18(2), 107 – 124.

Watts, P., and Grilli, S. T. (2003). "Underwater landslide shape, motion, deformation, and tsunami generation." *Proc., 13th Offshore and Polar Engineering Conf., Intl. Soc. of Offshore and Polar Engineers*, Cupertino, Calif., 3, 364 – 371.

Watts, P. (2004). "Probabilistic prediction of landslide tsunamis off Southern California." *Marine Geology*, 203, 281 – 301.

Wiegel, R.L. (1955). "Laboratory studies of gravity waves generated by the movement of a submarine body." *Trans. Am. Geophys. Union*, 36(5), 759 – 774.

Yuk, D., Yim, S.C., Liu, P.L.F. (2006). "Numerical modeling of submarine mass-movement generated waves using RANS model." *Computer & Geosciences*, 32, 927 – 935.

APPENDIX A

```
DO  j = 1, Nc

  Ω'(j)=0

   DO k=1,Nc

      tΩ (j,k) = abs(ts(j) - ts(k))*delay          !Eq.(39)

      Ω'(j) = Ω'(j) + Sw(k)*(1/(1+ tΩ(j,k)))       !Eq.(40)

      Ω(j,k) = Ω'(j)

   ENDDO

ENDDO
```

APPENDIX B

```
DO n=1,nt
  h_p=ho
  ellip=0.0

  DO j=1,Nc  !Evaluate each slide chunk
    ds=0  !Set initial horizontal displacement

    DO m=1,n  !Determine slide velocity

      IF (t(m)>=ts(j)) THEN  !Compare current time to onset time
        u_c=u_t*tanh((t(m)-ts(j))/t_o!Velocity evolution-Eq.(45)
      ELSE
        u_c=0  !Slide remains stationary for t<ts
      ENDIF

      ds=ds+u_c*dt  !Horizontal displacement – Eq.(46)

    ENDDO

    !Slide spatial location parameters
    x_c=x_o_I(j)+ds*cos(α)  !Center of mass motion – Eq.(47)
    x_l=x_c-0.5*b(j)*cos(α)  !Left end – Eq. (29)
    x_r=x_c+0.5*b(j)*cos(α)  !Right end – Eq. (30)

    DO ii=1,nx  !Delineate slide over x-domain

      ellip(ii)=mass_ratio*Δh*0.25*(1+tanh((x(ii)-x_l)/(S_f)))*(1-tanh((x(ii)-
                          x_r)/(S_f)))  !Slide delineating function - Eq.(43)

      h_p(ii)=h_p(ii)-ellip(ii,j) !Record the passage of individual slide chunks and
                                   reuse when modeling next chunk-
                                   Eq.(48)
    ENDDO
  ENDDO

  h_Nc(:,n)=h_c !Store water depth at t=t(n)created by Nc slides – (Eq. 49)

ENDDO
```

VITA

Arturo Jimenez Martinez received his Bachelor of Science degree in civil engineering from Jackson State University in 2009. He enrolled in the Ocean Engineering program at Texas A&M University in September 2009 and received his Master of Science degree in August 2011. His short term goal is to work in the industry as a coastal engineer and obtain a professional license. He plans to publish the investigation presented in this manuscript in the Journal of Waterway, Port, Coastal, and Ocean Engineering.

Mr. Jimenez Martinez may be reached at Moffat & Nichol Engineers, 11011 Richmond Avenue, Houston, TX 77042. His email is artur0_jm@hotmail.com.